



Influence of weather situation on non-CO₂ aviation climate effects: the REACT4C climate change functions

Christine Frömming¹, Volker Grewe^{1,2}, Sabine Brinkop¹, Patrick Jöckel¹, Amund S. Haslerud³, Simon Rosanka^{1,2,a}, Jesper van Manen^{1,2,b}, and Sigrun Matthes¹

¹Deutsches Zentrum für Luft- und Raumfahrt, Institut für Physik der Atmosphäre, Oberpfaffenhofen, Germany

²Delft University of Technology, Aerospace Engineering, Section Aircraft Noise and Climate Effects, Delft, the Netherlands

³Center for International Climate and Environmental Research – Oslo (CICERO), Oslo, Norway

^anow at: Forschungszentrum Jülich GmbH, Institute of Energy and Climate Research, IEK-8: Troposphere, Jülich, Germany

^bnow at: Ministry of Infrastructure and Water Management, The Hague, the Netherlands

Correspondence: Christine Frömming (christine.froemming@dlr.de)

Received: 30 May 2020 – Discussion started: 18 August 2020

Revised: 5 March 2021 – Accepted: 1 April 2021 – Published: 16 June 2021

Abstract. Emissions of aviation include CO₂, H₂O, NO_x, sulfur oxides, and soot. Many studies have investigated the annual mean climate impact of aviation emissions. While CO₂ has a long atmospheric residence time and is almost uniformly distributed in the atmosphere, non-CO₂ gases and particles and their products have short atmospheric residence times and are heterogeneously distributed. The climate impact of non-CO₂ aviation emissions is known to vary with different meteorological background situations. The aim of this study is to systematically investigate the influence of characteristic weather situations on aviation climate effects over the North Atlantic region, to identify the most sensitive areas, and to potentially detect systematic weather-related similarities. If aircraft were re-routed to avoid climate-sensitive regions, the overall aviation climate impact might be reduced. Hence, the sensitivity of the atmosphere to local emissions provides a basis for the assessment of weather-related, climate-optimized flight trajectory planning. To determine the climate change contribution of an individual emission as a function of location, time, and weather situation, the radiative impact of local emissions of NO_x and H₂O to changes in O₃, CH₄, H₂O and contrail cirrus was computed by means of the ECHAM5/MESSEy Atmospheric Chemistry model. From this, 4-dimensional climate change functions (CCFs) were derived. Typical weather situations in the North Atlantic region were considered for winter and summer. Weather-related differences in O₃, CH₄, H₂O, and contrail cirrus CCFs were investigated. The follow-

ing characteristics were identified: enhanced climate impact of contrail cirrus was detected for emissions in areas with large-scale lifting, whereas low climate impact of contrail cirrus was found in the area of the jet stream. Northwards of 60° N, contrails usually cause climate warming in winter, independent of the weather situation. NO_x emissions cause a high positive climate impact if released in the area of the jet stream or in high-pressure ridges, which induces a south- and downward transport of the emitted species, whereas NO_x emissions at, or transported towards, high latitudes cause low or even negative climate impact. Independent of the weather situation, total NO_x effects show a minimum at ~ 250 hPa, increasing towards higher and lower altitudes, with generally higher positive impact in summer than in winter. H₂O emissions induce a high climate impact when released in regions with lower tropopause height, whereas low climate impact occurs for emissions in areas with higher tropopause height. H₂O CCFs generally increase with height and are larger in winter than in summer. The CCFs of all individual species can be combined, facilitating the assessment of total climate impact of aircraft trajectories considering CO₂ and spatially and temporally varying non-CO₂ effects. Furthermore, they allow for the optimization of aircraft trajectories with reduced overall climate impact. This also facilitates a fair evaluation of trade-offs between individual species. In most regions, NO_x and contrail cirrus dominate the sensitivity to local aviation emissions. The findings of this study recommend

considering weather-related differences for flight trajectory optimization in favour of reducing total climate impact.

1 Introduction

Emissions of aviation include carbon dioxide (CO_2), water vapour (H_2O), nitrogen oxides (NO_x), sulfur oxides (SO_x), and soot. Furthermore, aviation emissions cause the formation of contrails and contrail cirrus. CO_2 and H_2O are greenhouse gases; their emissions cause a climate warming. Emissions of NO_x cause a short-term production of ozone (O_3) and a long-term reduction of methane (CH_4). Changes of the O_3 precursor CH_4 cause a secondary, long-term reduction of O_3 , which is called the primary mode ozone (PMO) effect. Both O_3 and CH_4 are greenhouse gases, for which an enhancement causes a climate warming, while a reduction causes a cooling. Contrails form when hot and moist exhaust mixes with ambient air, while they only persist if the ambient air is saturated with respect to ice. Persistent contrails may evolve into contrail cirrus, which have a lifetime of up to many hours. On average, contrails and contrail cirrus cause a climate warming; however in certain situations, they can also cause a cooling. Emissions of aerosols or aerosol precursors have a direct effect on climate, which can be warming (soot) or cooling (SO_x). Aviation aerosol emissions also have an indirect effect on clouds, which is still uncertain; thus the effect of aerosols has not been included in the present study. The most prominent climate effects of aviation emissions, their climate impact in terms of radiative forcing, its uncertainty, and the level of scientific understanding have been summarized by, for example, Lee et al. (2010, 2021) and Brasseur et al. (2016).

The CO_2 emissions from aviation contribute 1.6 % to the net anthropogenic effective radiative forcing. Taking the non- CO_2 effects into account, aviation constitutes 3.5 % of the total anthropogenic climate impact (in terms of effective radiative forcing; Lee et al., 2021). Compared with other modes of transportation, 12 % of the CO_2 emissions from global transportation are caused by aviation (Brasseur, 2008). This share is expected to increase, as the aviation sector has grown at an annual rate of 1.1 % over the last decade (Lee et al., 2021), while other sectors reduce their CO_2 emissions. However, future emissions are uncertain, and the uncertainty has increased due to reduced operations because of the COVID-19 pandemic (e.g. Friedlingstein et al., 2020; Le Quere et al., 2020). The Paris Agreement set the ambitious goal to keep the global temperature rise within this century well below 2°C compared to pre-industrial levels. In regard to this ambitious goal, political and societal pressure for sustainable aviation is increasing. Mitigation options, which may enable the aviation sector to reduce its climate impact, ought to be identified and evaluated.

Mitigation options may involve technological measures, such as alternative fuels, novel engine concepts, modification of aircraft design, or policy measures such as emission trading or emission reduction schemes, for instance the EU ETS (Emissions Trading System; European Commission, 2015) or CORSIA (Carbon Offsetting and Reduction Scheme for International Aviation; ICAO, 2020), or technology targets like the ACARE (Advisory Council for Aviation Research and Innovation in Europe) Vision 2020 and Flight-path 2050 (ACARE, 2020). Another efficient possibility for mitigation may be operational measures, e.g. identifying alternative flight trajectories with reduced climate impact. CO_2 with its long atmospheric residence time is almost uniformly distributed in the atmosphere, and its climate impact is independent of the location and situation during its release. The non- CO_2 gases, particles and their products, which comprise 2/3 of the aviation net effective radiative forcing (Lee et al., 2021), however, have shorter atmospheric residence times and are heterogeneously distributed in the atmosphere. More precisely, the effects of non- CO_2 emissions depend on chemical and meteorological background conditions during their release, which vary with geographic location (e.g. Köhler et al., 2013), altitude (e.g. Frömming et al., 2012), time, local insolation (e.g. Gauss et al., 2006), and actual weather. Thus, regions and times which are more sensitive to non- CO_2 aviation emissions can be identified. If aircraft trajectories avoid these areas with enhanced sensitivity, aviation climate impact can potentially be mitigated (e.g. Matthes et al., 2012; Grewe et al., 2014a). Such operational measures might be implemented much faster than technological improvements, which require much more time for research, development, and implementation.

Previous studies investigated the annual or seasonal mean impact on contrail formation and related radiative forcing by permanent changes in flight altitudes or lateral changes of flight routes (e.g. Sausen et al., 1998; Fichter et al., 2005; Rädcl and Shine, 2008; Frömming et al., 2012; Matthes et al., 2021). Others tried to avoid contrails and contrail cirrus by situation-related small changes in flight levels when flying through contrail regions (e.g. Mannstein et al., 2005; Chen et al., 2012), or they calculated horizontal flight trajectory changes to reduce travel time through contrail formation regions (Sridhar et al., 2011). These studies found considerable potential for the reduction of contrails, but related trade-offs were considered only by means of different metrics (e.g. fuel consumption versus travel time through contrail regions) or not at all. Irvine et al. (2014) presented a framework for the consistent assessment of maximum extra distance to be added to a flight for avoiding contrails without generating an increase in overall climate impact, finding a high dependency on the metric, time horizon, and aircraft type. Zou et al. (2016) considered both horizontal and vertical aircraft trajectory changes and minimized the total flying cost of fuel consumption, CO_2 emissions, travel time, and contrail formation by converting the climate impacts and other resulting trade-

offs into monetary value. Climate impacts were considered in terms of global warming potential (GWP); thus a strong dependence on the time horizon was found. A study by Hartjes et al. (2016) determined 3-dimensional aircraft trajectories while minimizing contrail formation and found vertical trajectory adjustments to be preferable over horizontal trajectory changes. Until now, the spatial and temporal variability of climate effects from aircraft emissions of NO_x on O_3 and CH_4 has mainly been considered in terms of climatological effects by means of permanent changes of flight altitudes or routes (Gauss et al., 2006; Köhler et al., 2008, 2013; Fichter, 2009; Frömming et al., 2012; Matthes et al., 2021). Grewe and Stenke (2008) and Fichter (2009) systematically investigated annual mean effects of unified emissions on O_3 , CH_4 , H_2O , and contrails in terms of their altitudinal and latitudinal dependency, by identifying regions where emissions have the largest impact in a climatological sense.

However, none of these previous studies considered the impact of various aviation effects in relation to the actual weather situation, location, and altitude in detail. Within the project REACT4C (<https://www.react4c.eu/>, last access: 9 June 2021), the feasibility of optimizing flight altitudes and flight routes for minimum climate impact was explored as a function of the actual weather situation (Matthes et al., 2012). The North Atlantic region was chosen as a study domain because flight trajectories are not as constrained as over the continents. There are long-distance flights which allow detours and sufficient air traffic to be studied, making it worthwhile to study re-routing. Furthermore, the traffic is not too dense to enable re-routing without generating too many conflicts with other flights. Additionally, this study region is characterized by synoptical-scale archetypical weather patterns, which allow a set of representative weather situations to be created. Initial studies of the REACT4C project established the consideration of different weather situations with respect to aviation climate impact. Irvine et al. (2013) defined characteristic weather patterns in the North Atlantic and defined proxies for the climate impact of carbon dioxide, ozone, water vapour, and contrails to facilitate climate optimal aircraft routing. Grewe et al. (2014b) presented and verified the modelling concept of REACT4C, introducing the calculation of climate change functions (CCFs), which are a measure for the climate impact of a local emission (see Sect. 2). Grewe et al. (2014a) displayed local aviation climate effects exemplarily, pointed out consequences for climate-optimized aircraft trajectories, and showed the climate impact reduction potential for one specific weather pattern. Rosanka et al. (2020) presented a process-based analysis of weather-dependent aviation NO_x -effects. The present study covers the entire ensemble of REACT4C climate change functions (CCFs) for eight representative weather situations in the North Atlantic region for winter and summer. The altitude, location, and weather dependency of aviation climate effects of O_3 , CH_4 , H_2O , and contrail cirrus are presented, discussed, and validated. The distribution of high or low sen-

sitivity to aviation emissions for all species is systematically examined. Thus, the present study represents the fundamental data basis of most REACT4C-related studies. Further associated studies are based on the ensemble of these CCFs, e.g. for the development of more generic algorithmic CCFs (see Sect. 6), which enable the calculation of climate impact by means of meteorological key parameters (e.g. Matthes et al., 2017; Yin et al., 2018b; Van Manen and Grewe, 2019). Subsequent studies complete the range of REACT4C-related publications focussing on the climate impact reduction potential, utilizing either REACT4C CCFs or algorithmic CCFs for operational mitigation through climate-optimized aircraft trajectories (e.g. Grewe et al., 2017; Matthes et al., 2020; Lührs et al., 2021).

In the present study, first the methodology of calculating the weather-related impact of a local emission on climate in a comprehensive climate chemistry model is presented (Sect. 2). The weather situations which were used in the present study are described in Sect. 3. An overview on the experimental setup is given in Sect. 2.5. The resulting climate change functions (CCFs) are presented in Sect. 4. The results are discussed, and an outlook is given on how the CCFs could be used for the planning of climate-optimized aircraft trajectories (Sect. 5). Section 6 concludes with a short summary and ideas for future studies.

2 Model description

The ECHAM/MESSEy Atmospheric Chemistry Model (EMAC; Jöckel et al., 2010, 2016) is a numerical chemistry climate model system which implements submodels describing physical and chemical atmospheric processes, ranging from the troposphere up to the middle atmosphere, and their interactions with the biosphere, hydrosphere, and geosphere. The Modular Earth Submodel System (MESSy) couples the various submodels to the core atmospheric model ECHAM5 (Roeckner et al., 2006). The chemistry is calculated by the submodel MECCA (v3.2, Sander et al., 2011). Non-methane hydrocarbon (NMHC) chemistry is employed, reproducing the main features of the tropospheric chemistry (Houweling et al., 1998). A Lagrangian transport scheme is employed within this study using the submodel ATTILA (Reithmeier and Sausen, 2002; Brinkop and Jöckel, 2019). Further, two newly developed submodels were employed within the present study, the submodels AIRTRAC and CONTRAIL (Grewe et al., 2014b). EMAC is used in a T42L41 spectral resolution, corresponding to a quadratic Gaussian grid of $\sim 2.8^\circ \times 2.8^\circ$ in latitude and longitude and 41 vertical layers from the surface to 5 hPa, which is a compromise between the level of detail within the simulation and the computational expense.

2.1 Model setup for calculating climate change functions

Within this study, EMAC is employed to calculate the atmospheric impact of standardized air traffic emissions on the chemical composition of the atmosphere and on the formation of contrails and contrail cirrus at predefined longitudes, latitudes, altitudes, and times. The location- and time-dependent specific climate impacts per emission are referred to as climate change functions (CCFs). The CCFs are a measure for the sensitivity of a certain emission location to aviation climate impact as introduced by Matthes et al. (2012). These CCFs enable the assessment of re-routing options with reduced climate impact. Hence, in this study we present a numerical modelling approach for calculating climate change functions with the modular global chemistry climate model EMAC. In order to quantify this spatially and temporally dependent climate impact information, it is necessary to calculate the atmospheric impact in terms of concentration changes and associated radiative impact of a specific emission at the given geographic position, altitude, and time of emission. We use a Lagrangian scheme (ATTILA) in the modular Earth system model EMAC in order to numerically simulate the fate of emissions on Lagrangian trajectories and quantify associated atmospheric impacts, concentration changes, and radiative impacts in terms of radiative forcing. This radiative forcing is translated to a climate metric in order to quantify the climate impact. By remapping these impacts quantified with EMAC to the specific location and time of emission, we construct 4-dimensional climate change functions. For a detailed description of the methodology, we refer to the companion model development paper of Grewe et al. (2014b), while in the present study we review only the relevant information and focus on the results.

2.2 Chemical changes

To derive the CCFs, a 4-dimensional time-region grid is defined. This time-region grid covers cruise-altitude-relevant pressure levels from 400 to 200 hPa over the North Atlantic area (between 30 and 80° N and between 80 and 0° W), in total yielding 168 grid points (see Table 1). At each of these time-region grid points, a pulse emission of NO_x (5×10^5 kg NO) and H₂O (1.25×10^7 kg H₂O) is released by means of the submodel TREXP (Tracer Release EXperiments from Point sources) within one model time step of 15 min. A Lagrangian approach was chosen as it facilitates the calculation of CCFs for a number of time regions within a single EMAC simulation. The tracer concentration from the pulse emission is equally distributed on 50 air parcel trajectories, which are (randomly distributed) started from within the EMAC grid box in which the time-region grid point lies. The air parcel trajectories are advected by the submodel ATTILA using the wind field from EMAC. Diffusive processes through inter-parcel mixing of air parcel trajectories with

tracer loading with, for example, empty background trajectories ($\sim 169\,000$ in the Northern Hemisphere) are parameterized by means of the submodel LGTMIX. The mixing of adjacent parcels is represented by slightly changing the mass mixing ratio c_i in a parcel towards the average mixing ratio of all parcels within one grid box \bar{c} . The new mixing ratio of the air parcel is then calculated by $c_i^{\text{new}} = c_i + (\bar{c} - c_i)d$, with d being a dimensionless mixing parameter within the range [0, 1], controlling the magnitude of exchange (Reithmeier and Sausen, 2002; Brinkop and Jöckel, 2019). NO_x emissions influence the production and loss of O₃ and the loss of CH₄ via the partitioning of OH and HO₂. For each air parcel trajectory, the contribution of the pulse emission to the atmospheric composition is calculated by the newly developed submodel AIRTRAC (Grewe et al., 2014b). AIRTRAC solves a simplified set of chemical equations on the air parcel trajectories (see Grewe, 2013) using the diagnosed production (P) and loss (L) terms from the kinetic solver (MECCA) of the background chemistry, while the proportional contributions of the emitted species to the atmospheric mixing ratios of NO_y (all active nitrogen species), HNO₃, O₃, HO₂, OH, and CH₄ are calculated for each air parcel trajectory. Therefore the emissions need to be partitioned into background emissions (b) and additional emissions (e). The ozone production for additional emissions ($P_{\text{O}_3}^e$) via reaction



is calculated (according to Grewe et al., 2010):

$$P_{\text{O}_3}^e = P_{\text{O}_3}^b \cdot \frac{1}{2} \left(\frac{\text{HO}_2^e}{\text{HO}_2^b} + \frac{\text{NO}^e}{\text{NO}^b} \right). \quad (1)$$

The reaction rate for ozone loss from additional emissions ($L_{\text{O}_3}^e$) via reaction



is calculated similarly:

$$L_{\text{O}_3}^e = L_{\text{O}_3}^b \cdot \frac{1}{2} \left(\frac{\text{NO}_2^e}{\text{NO}_2^b} + \frac{\text{O}_3^e}{\text{O}_3^b} \right). \quad (2)$$

This exemplarily demonstrates the methodology of calculating the atmospheric changes attributed to the additionally emitted species; further details are elaborated in Grewe et al. (2014b). An analogous approach is used for CH₄, while taking into account the most relevant reactions with regard to OH and HO₂. Atmospheric processes, such as wash-out and dry deposition, are also proportionally taken into account on the air parcel trajectories. For H₂O emissions, only loss processes are considered. The loss processes affecting the additionally emitted H₂O are included proportionally to the precipitation rate (Grewe et al., 2014a). Figure 1 shows exemplarily the temporal evolution of the contributions from NO_x emissions for one arbitrary time region to the NO_x, O₃ and CH₄ atmospheric burden. NO_x is completely washed out

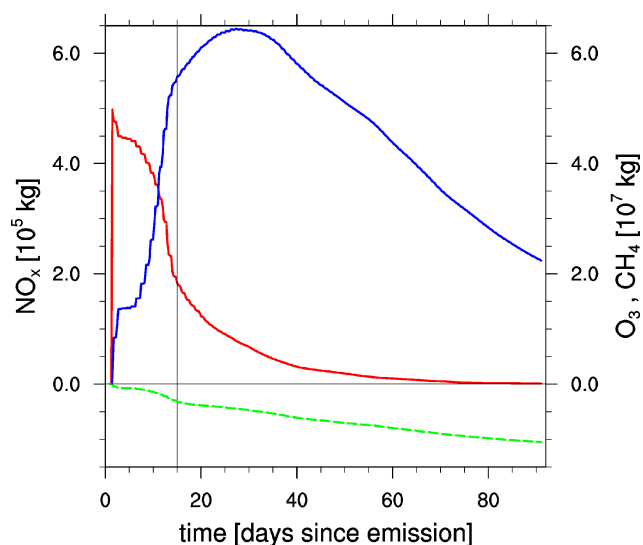


Figure 1. Temporal evolution of the contribution to the global atmospheric mass of NO_x (red), O_3 (blue), and CH_4 (green) attributed to the emissions in one arbitrary time region within 90 d after emission.

within the first 30–40 d. O_3 increases while additional NO_x is available, then the O_3 loss dominates, and O_3 reduces gradually. At the same time, CH_4 is reduced due to an increase in OH, which is caused by additional NO_x first and by additional O_3 later. The calculation of chemical contributions from time-region emissions is accomplished on the air parcel trajectories, i.e. in Lagrangian space. The background information required for the chemical calculation is transferred from grid point space to Lagrangian space.

2.3 Contrails and contrail cirrus

Contrails may form in the atmosphere if the ambient air is cold and moist enough, and they may persist if the air is supersaturated with respect to ice (Schumann, 1996) and evolve into contrail cirrus. Within this study, we do not distinguish between linear contrails and contrail cirrus. In EMAC the atmospheric ability to form persistent contrails and contrail cirrus is calculated at each time step according to Burkhardt et al. (2008) and Burkhardt and Kaercher (2009). This atmospheric ability is referred to with the term “potential contrail coverage”. The potential contrail coverage indicates the fraction of a grid box which can be covered by contrails at maximum. The potential contrail coverage and the background properties, which are required for the contrail calculations, are transferred onto the air parcel trajectories. Then the actual contrail coverage is determined with a dependency on whether air traffic occurs in the respective grid box. This is true for the respective time region, where one pulse of air traffic emissions initiates the formation of contrails. Their temporal development according to spreading, sublimation, and sedimentation of ice particles is parameterized as fol-

lows. The prognostic equation for contrail coverage is the sum of newly formed contrails and spread contrails from preceding time steps:

$$\frac{db}{dt} = \left(\frac{db}{dt}\right)_{\text{new}} + \left(\frac{db}{dt}\right)_{\text{spread}} \quad (3)$$

The coverage of newly formed contrails is determined from initial contrail dimensions (width and length of the contrail in EMAC grid box), while the spreading is parameterized depending on the vertical wind shear according to Burkhardt and Kaercher (2009) (see Grewe et al., 2014b). Contrails are characterized through their coverage (b) and their water mixing ratio (m). The prognostic equation for contrail ice water mixing ratio m includes the formation of new contrails, sedimentation of ice, deposition of water vapour on contrail ice particles, and sublimation (Burkhardt and Kaercher, 2009).

$$\frac{dm}{dt} = \left(\frac{dm}{dt}\right)_{\text{new}} + \left(\frac{dm}{dt}\right)_{\text{sed}} + \left(\frac{dm}{dt}\right)_{\text{dep/subl}} \quad (4)$$

The newly formed ice water depends on the condensation rate in the contrail-covered part of the grid box (Ponater et al., 2002), the sedimentation of ice is parameterized according to the divergence of the flux of ice particles according to Heymsfield and Donner (1990), and the sublimation and growth depend on the tendency of potential contrail coverage. Further details are given by Grewe et al. (2014b).

2.4 Radiative forcing and climate change functions

The radiative transfer calculations are accomplished in grid point space; therefore the properties of air parcel trajectories are transferred from Lagrangian space to grid point space. The approach described in the previous sections and given in more detail in Grewe et al. (2014a) leads to a 4-dimensional distribution of mixing ratios of trace gases, coverage, and optical properties of contrails, which are caused by a local pulse emission over an integration time of 90 d (in the case of chemical perturbations) or 3 d (in the case of contrails and contrail cirrus). The 90 d cover most of the short-term responses resulting from NO_x emissions, while longer term responses are projected by extrapolation. The impact of the perturbations is quantified by means of radiative forcing (RF), the radiation imbalance at the tropopause caused by radiatively active species (Shine et al., 1990). Positive RF will lead to climate warming and vice versa. The instantaneous radiative forcing at the tropopause is calculated directly within the submodel RAD4ALL (Dietmüller et al., 2016) for O_3 , H_2O , and contrails. The stratosphere-adjusted RF, which allows stratospheric temperatures to adjust to the new equilibrium following the radiative imbalance, is derived from the instantaneous RF as described in detail by Grewe et al. (2014b). The RF from CH_4 is determined from the CH_4 mass perturbation following the method described by Shine et al. (1990). The RF from primary mode O_3 (PMO) is derived by applying a constant factor of 0.29 to the CH_4 RF

Table 1. Overview of the time-region grid points, where standardized emissions are released and specific local climate change functions are calculated.

Latitudes [° N]	80	60	50	45	40	35	30
Longitudes [° W]	75	60	45	30	15	0	
Pressure levels [hPa]	200	250	300	400			

(Dahlmann, 2012). The adjusted H₂O RF is calculated based on results from Grewe and Stenke (2008), employing their relationship between H₂O mass and adjusted RF. Because of its long perturbation lifetime, emissions of CO₂ are assumed to be equally mixed within the atmosphere. The temporal evolution of the change in mixing ratio is calculated following Fuglestedt et al. (2010) and Forster et al. (2007). The RF calculation for CO₂ includes a simple linearized conversion factor between the change in its atmospheric mass and the RF as given by Grewe et al. (2014b). Regarding contrails, the difference between the adjusted and the instantaneous RF is marginal (Marquart et al., 2003); hence within the present study, the instantaneous RF is used. Because of the overall setup of the experiment, in some cases very small ice water contents were simulated. Several other radiation parameterizations are limited to ice water contents or optical depths (τ) exceeding a certain threshold (Ruben Rodriguez de Leon, Manchester Metropolitan University, personal communication, 2018). Although for the model used here, no such validity range exists, in the present study, only contrails with $\tau \geq 0.01$ are included, as it is suspected that, in some cases, very small optical depths in combination with small coverages may not yield correct shortwave radiative forcings.

From RF various climate metrics can be derived by means of simple climate response functions. Different climate metrics aim to answer different political questions. As the main components of climate metrics (RF and ΔT , global mean temperature change) are accumulative and annually variable, averaged or time-integrated climate metrics are favourable. They evaluate mean impacts over an integration period and are less sensitive to lifetime. A suitable climate indicator is the averaged global mean temperature change integrated over a certain time horizon H , i.e. the average temperature response (ATR; Schwartz Dallara et al., 2011), or similarly the average integrated absolute global temperature potential (iAGTP), divided by the time horizon H (Aamaas et al., 2013). Here, we calculate the average global mean temperature change following Aamaas et al. (2013) for a pulse emission integrated over a time horizon of 20 years, as we focus on the short-term effect of a climate-optimized re-routing strategy. Based on the RF calculations, other climate metrics could be calculated for other time horizons, e.g. 20, 50, or 100 years (Fuglestedt et al., 2010), such as the absolute global warming potential (AGWP) or the absolute global temperature potential, not only for pulse but also for sustained emissions or future emission scenarios, which would give a wide range of CCFs. A temperature-based climate

metric has the advantage that it is not only used within the climate modelling community, but also understood by non-experts. A discussion on the suitability of various metrics and time horizons regarding different research questions (e.g. pulse versus sustained emissions) is given by Grewe et al. (2014b) and Grewe and Dahlmann (2015).

2.5 Experimental setup

For the calculation of the 4-dimensional climate change functions, predefined emissions are released in each time region and distributed on a set of 50 Lagrangian air parcel trajectories. The emission regions as listed in Table 1 comprise 168 locations (6 longitudes \times 7 latitudes \times 4 pressure levels). For each emission location, the emission impact calculations were performed using the global chemistry climate model EMAC for episodic simulations. As the intention was to investigate to what extent the local aviation climate effects change during the course of the day, three emission times (06:00, 12:00, and 18:00 UTC) were considered. A total of 15 time regions could be comprised within one simulation. Thus for the 4032 time regions in total (168 grid points \times 3 emission times \times 8 weather situations), plus one simulation for spin-up and definition of characteristic weather patterns, a total of ~ 270 simulations were performed, using 13 500 CPU hours. The spin-up period was 6 months; a further 18 months was used for the identification of the characteristic weather situations in EMAC. The year 2000 was simulated, including assumptions for background emissions for that year (e.g. Hoor et al., 2009). The definition period was used to match EMAC model weather situations with characteristic weather patterns as defined by Irvine et al. (2013) from ECMWF Interim reanalysis data. A model date was selected for each of the characteristic weather situations for winter and summer, respectively. For example, 23 December in 2000 in EMAC was found to match with weather pattern W1 from Irvine et al. (2013) in ERA Interim. The selected dates from the definition period were used for restarting the model to simulate the characteristic weather situation for the integration period. Model dates were chosen, where the selected weather pattern remained rather stable for the following 3–5 d. Then other weather situations followed. Within this study we performed quasi-chemical-transport model (QCTM) simulations (Deckert et al., 2011). These simulations are dedicated to ensure that the changes from the time-region emissions do not feed back to the base model processes, and identical background meteorology and chemistry is guaranteed

for the spin-up and definition phase and for all time-region simulations. The contrail RF was calculated for 3 d after the emission occurred; after this period no contrails remained, while the RF for NO_x , CH_4 , and H_2O was calculated for 3 months after the emission occurred. Most effects faded out during that period; however, effects which were still going on were extrapolated.

3 Weather situations

Figure 2 shows eight representative weather situations in the North Atlantic, as determined within the EMAC model. These typical weather situations were defined according to the classification of Irvine et al. (2013). They represent the variability in the North Atlantic in winter and summer. The patterns were determined by their similarity to the North Atlantic Oscillation (NAO) and East Atlantic (EA) teleconnection patterns and can be characterized by the strength and position of the jet stream. Five specific types are defined in wintertime. Weather situation W1 shows a strong zonal jet stream, and a low-pressure trough is dominating the North Atlantic. Weather situations W2 and W3 represent a meridionally tilted jet stream, with either a weaker or stronger jet, respectively. Weather situation W4 is characterized by a ridge over the eastern North Atlantic, and the jet is confined to the western part of the North Atlantic. W5 shows the least similarity to the NAO and EA teleconnection patterns, and the jet is weak and confined to the US coast. W5 is the most frequent weather situation in winter (26 d per season). Types W1 to W4 occur on average 15–19 d per winter (Irvine et al., 2013). In summer, only three types are defined because of weaker teleconnection patterns and a smaller variability of the jet. Weather pattern S1 represents a strong zonal jet stream, although the jet is weaker than in winter. Weather pattern S2 is characterized by a jet which is weakly tilted towards northeast. Weather pattern S3 shows a weak but strongly tilted jet. Weather patterns S1 and S3 occur with similar frequency (19 and 18 d per summer, respectively). S2 is the most frequent type in summer (55 d per summer). For each of these eight weather situations, a representative model date is selected, for which the weather-dependent climate change functions were calculated. Results of CCFs for one specific weather situation (W1) were exemplarily shown by Grewe et al. (2014a). Here, an overview of the climate change functions for all representative winter and summer weather situations is presented and analysed in detail, with particular focus on the differences between the weather situations.

4 Climate change functions

The climate change functions were calculated for all time regions by means of episodic simulations with the global chemistry climate model EMAC. For every time region, the development of contrails, the decay of H_2O , and the production and loss of O_3 , CH_4 , PMO, and other trace gases were calculated as described in Sect. 2, and the respective radiative forcing and the average global temperature response for a time horizon of 20 years (ATR20) were determined. This means that for every time region and every species, one global number results, which refers to the original emission location. In the figures which are shown in the following section denoted as climate change functions, these global numbers are plotted at the location of the corresponding time region, i.e. where the original emission took place (although the colour-coded value represents a global effect). In other words, if emissions are released at a time region where CCFs show a high sensitivity (colour-coded in red in the CCF; Figs. 7, 8, 11, and 12), these emissions cause a high global climate impact, whereas emissions released at locations with low CCF values (e.g. light yellow or even blue in these Figures) cause low or even negative global climate impact (cooling). Within this research paper, we exemplarily show CCFs for the 250 hPa level and an emission time of 12:00 UTC. The entire ensemble of CCFs derived within REACT4C for all species for four emission levels, three emission times and eight weather situations is presented in the Supplement.

We describe the potential contrail coverage and contrail cirrus CCF for all weather situations in Sect. 4.1, the CCFs for O_3 and the combined effects of O_3 and CH_4 (total NO_x) are presented in Sect. 4.2 and the CCFs for H_2O are described in Sect. 4.3.

4.1 Contrail effects

Figure 3 shows the potential contrail coverage for the eight representative winter and summer weather situations as simulated with the EMAC model. The potential contrail coverage indicates the probability of atmospheric conditions enabling the formation of persistent contrails. A potential contrail coverage which is non-zero in the time step of emission release in the respective time region is a prerequisite for a non-zero contrail CCF (shown in Fig. 7); only then can a contrail be formed. The magnitude and sign of the contrail CCF depend on the temporal development of contrail properties according to spreading, sublimation, and sedimentation and on environmental properties, e.g. natural clouds and solar insolation. When averaged over the year (not shown), maximum potential contrail coverage is found in the storm track region and over Greenland, whereas minimum potential coverage is found over Newfoundland. In our study region, the mean potential contrail coverage ranges from 20 %–36 % at 250 hPa between the weather situations. The actual magnitude and distribution of potential contrail coverage depend on

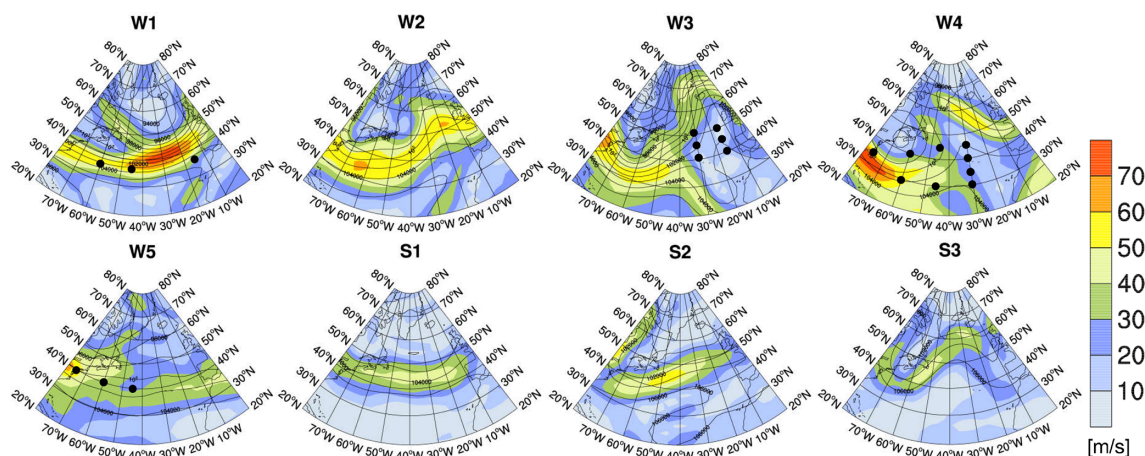


Figure 2. Geopotential height (black contours in gpm) and wind velocities in metres per second (ms^{-1} , colour bar) at 250 hPa for five representative winter weather situations (W1–W5) and three summer situations (S1–S3) as simulated with EMAC using the classification of Irvine et al. (2013). The black dots mark the regions discussed in Sect. 4.2 and listed in Table A1. Please note that the maps in Fig. 2 show a somewhat larger area for a better representation of the weather patterns than the maps showing the CCFs in Figs. 3, 7, 8, 11, and 12.

the season and weather situation. Highest potential coverages are found in weather situations W4, W5, and S2 between 250 and 300 hPa. Minimum contrail formation is found at 400 hPa, independent of the weather situation, since the temperature threshold for contrail formation is more frequently surpassed at that level, particularly at low latitudes. Common features found in the weather situations studied here are an enhanced potential contrail coverage in the vicinity of Greenland, where saturation is induced by orographic lifting. Enhanced potential contrail coverage can be found south of the jet stream (see Fig. 3, e.g. W1), where the tropopause is higher, and in areas with strong meridional transport, e.g. around ridges (e.g. W4), where air masses are lifted, which also leads to saturation. In contrast, comparably low potential coverages can be observed in the area of the jet stream (e.g. W1, W3).

As described in Sect. 2, aviation emissions are released in every time region in our study area, resulting in contrail coverage if atmospheric conditions allow for it. The contrail coverage and ice water content are transported on air parcel trajectories and evolve according to spreading, sedimentation, and sublimation. The span of contrail lifetimes ranges from 15 min to more than 24 h. A mean lifetime of contrails of 3.5 ± 5.3 h was found for all weather situations considered. In winter, contrails exist on average for 4.0 h, with mean lifetimes ranging from 1.9 h for W2 to over 5 h for W4 and W5. In summer, the mean lifetime of contrails is shorter (2.5 h) and similar for all weather situations. A total of 78 % of all contrails live less than 5 h, and only 7 % of all contrails live longer than 10 h. Contrail net RF is the sum of positive longwave and negative shortwave RF of similar magnitude (Ponater et al., 2002). Figure 4 shows the probability density function of contrail net RF, emphasizing that the majority of contrails within the present study cause a mean positive net

RF. The scatter plot of net RF versus contrail lifetime for all contrails in Fig. 5 shows that a negative net RF may only occur for contrails with lifetimes less than 10 h, independent of the weather situation. This is due to the fact that contrail RF may only be negative during daytime within a short time-frame (during and close to twilight; Meerkötter et al., 1999). The strong shortwave cooling during twilight is caused by the flat angle of incidence and a comparably longer path through the contrails and therefore a higher reflective impact (Meerkötter et al., 1999). The longer a contrail lives, the higher is the probability that a larger amount of its lifetime lies outside this timeframe. The scatter plot in Fig. 6 shows the instantaneous net radiative forcing relative to the actual, local daytime and night-time for all time steps over the whole contrail lifetime for all time regions for weather pattern W2. At night (net top solar radiation = 0, horizontally spread for better readability), contrails cause only positive net radiative forcing. During twilight and daytime with low incoming solar radiation (up to $\sim 500 \text{ W m}^{-2}$), the largest spread of net radiative forcing is found, which can be both positive or negative, resulting from positive longwave and negative shortwave RF of similar extent.

To enhance the spatial resolution of the contrail cirrus CCFs, the contrail RF, which is initially available on the resolution of the time region grid ($15^\circ \times 5\text{--}20^\circ$), is masked with the information of whether contrail cirrus formation is possible at all (i.e. the potential contrail coverage), which is available at the finer spatial resolution of the EMAC model ($\sim 2.8^\circ \times 2.8^\circ$). Figure 7 shows the climate change functions of contrail cirrus in terms of ATR20 for all weather situations exemplarily at 250 hPa for an emission time of 12:00 UTC. Contrail cirrus CCFs for other pressure levels and times are shown in the Supplement. Overall, the CCFs of contrail cirrus show a strong spatial and temporal variability and large

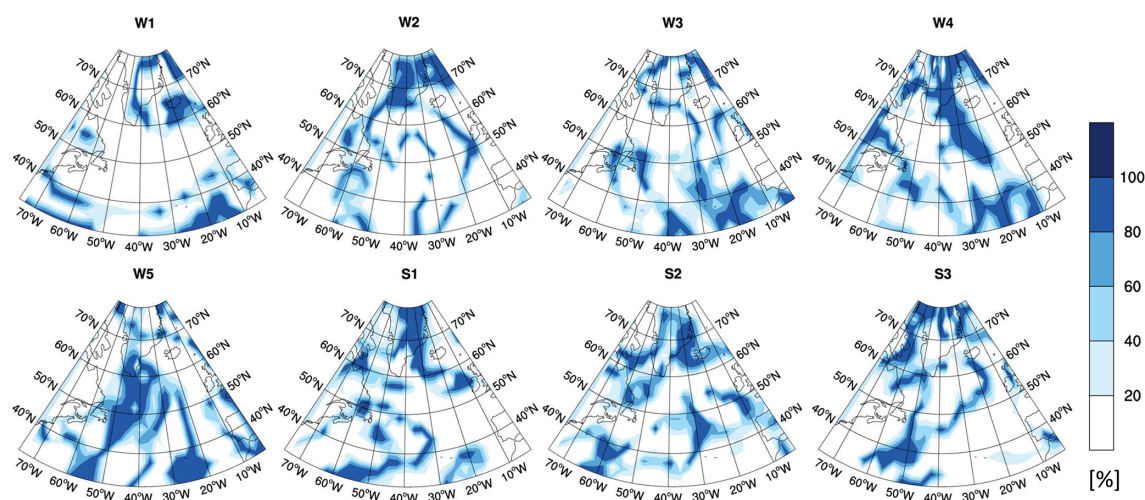


Figure 3. Potential contrail coverage at the time step of emission release (12:00 UTC) in percent (%) at 250 hPa for eight representative weather situations.

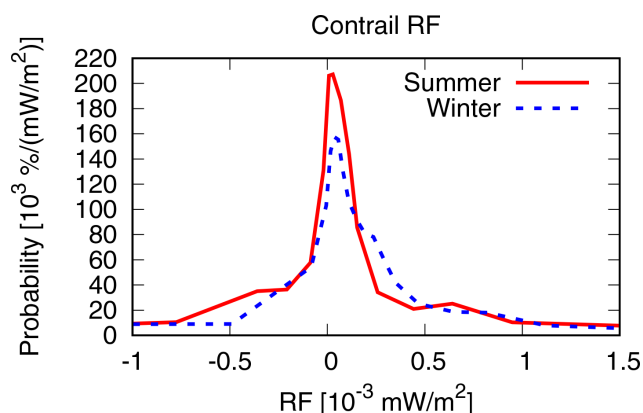


Figure 4. Probability density function of contrail net RF for winter and summer weather situations.

differences with respect to the various weather situations. In general, the climate impact of contrail cirrus may be either positive or negative, and the sign of the instantaneous radiative forcing can even change during their lifetime. On average the positive radiative forcing dominates within all weather situations, indicated by positive CCF values. In winter, all contrails northwards of 60° N have a warming climate impact as they are night-time contrails in most cases. Similarities which indicate a significant relationship between the weather situation and the CCFs are not easily identified, although we find a few characteristic features: an enhanced climate impact (irrespective of positive or negative) south of the jet stream, in the vicinity of Greenland, and in areas with strong meridional transport (e.g. around high-pressure ridges in W3 and W4). In contrast, close to the jet stream, comparably low contrail cirrus climate impact is found. Whether contrails have a positive or negative CCF depends mainly on

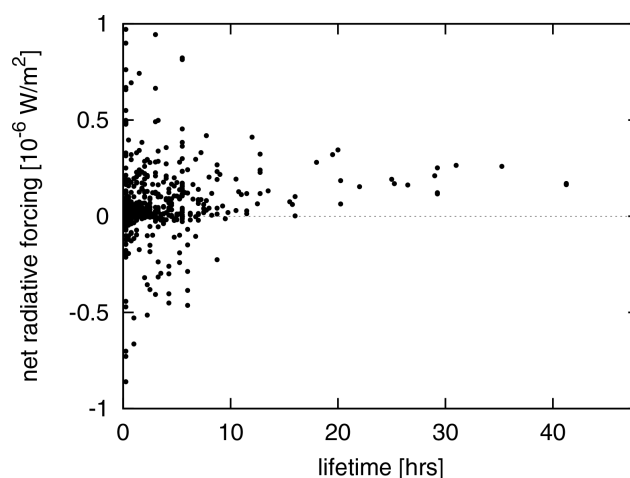


Figure 5. Instantaneous net radiative forcing of contrails relative to the contrail lifetime for winter and summer weather situations.

the solar insolation (day/night) during their entire lifetime. If contrails have a cooling climate effect, a considerable part of their lifetime must exist during daytime. Contrails which exist only during night time only have a warming effect. Hence, also the time of emission release is essential in combination with the contrail lifetime as these parameters have the potential to change the sign of contrail climate impact. This becomes apparent in the Supplement, where contrail cirrus CCFs for all emission times are shown. For example in W2, there is a warming contrail cirrus area in the eastern Atlantic at 06:00 UTC, which is night-time in that region. This CCF turns into a cooling contrail cirrus area for emissions at 12:00 UTC (early morning hours in that region), while for emissions at 18:00 UTC (afternoon), the CCF becomes positive again.

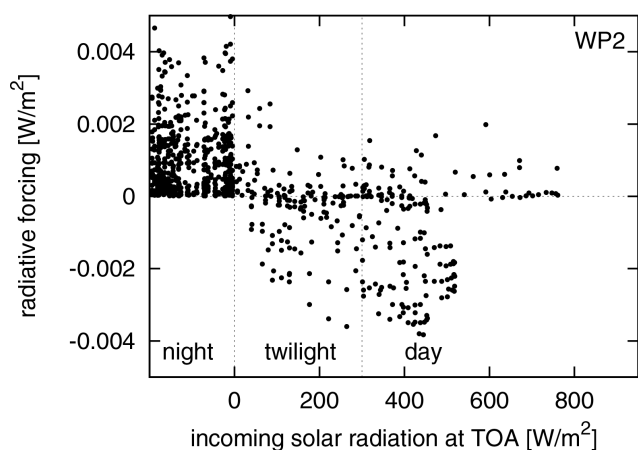


Figure 6. Instantaneous net radiative forcing at top of atmosphere (TOA) of individual contrails relative to the actual, local time (night, daytime, twilight) for weather pattern W2.

4.2 Nitrogen oxide effects

Figure 8 shows the climate change functions due to ozone (O_3) changes induced by aviation NO_x emissions. The O_3 CCF is always positive (i.e. a warming), and the spatial variabilities of the O_3 CCFs are significantly lower than those of contrail and contrail cirrus. The O_3 CCF patterns show distinct similarities to the weather pattern (Fig. 2). Larger O_3 CCF values are found in the area of the jet stream, e.g. at $35^\circ N$, $50^\circ W$ in W1, or in the area of the high-pressure ridges, e.g. reaching from the central or east Atlantic towards Iceland or Greenland in W2, W3, and W4, whereas low O_3 CCFs are found at high latitudes in the winter weather patterns and in the area of low-pressure troughs. These similarities between the weather patterns and the CCFs patterns indicate that the meteorological situation during the time of emission strongly influences the ozone production and thus the climate impact of the emitted NO_x . Our findings are supported by earlier climatological studies showing a higher O_3 response for NO_x emissions at low latitudes (e.g. Berntsen et al., 2005; Köhler et al., 2008; Grewe and Stenke, 2008). Gauss et al. (2006) found an amplified seasonal variation of O_3 effects for enhanced emissions at high northern latitudes. They found a reduction of O_3 for enhanced use of polar routes because of reduced or even absent photochemistry at high latitudes in winter but an increase in total O_3 for enhanced polar routes in summer because an increased fraction of emissions is released in the lowermost stratosphere, where NO_x accumulates more efficiently, yielding an increase in total O_3 burden.

To what extent different transport pathways affect the ozone production following an emission of NO_x is exemplarily illustrated in Fig. 9, showing the evolution of ozone for two neighbouring emission locations (A and B), both located at $45^\circ N$ but at different longitudes (30 and $15^\circ W$,

respectively) and in different relation to the high-pressure ridge in weather pattern W3. The air parcel starting at emission location A (left panel of Fig. 9) is west of the high-pressure ridge and stays at higher altitudes (above an altitude of 350 hPa in the first weeks) and at higher latitudes (northward of $30^\circ N$), whereas the air parcel starting at B, located in the high-pressure ridge, is transported southwards and downwards after emission and stays at $\sim 30^\circ N$ and below an altitude of ~ 300 hPa until the end of February. During that time, the ozone mixing ratio increases strongly and remains at around 30 to 40 $nmol\ mol^{-1}$, whereas the air parcel starting at A (west of the high-pressure ridge) experiences only moderate ozone production because of the scarce availability of sunlight at high latitudes in January and February, yielding an ozone mixing ratio of only 15 to 20 $nmol\ mol^{-1}$. This example demonstrates the importance of the emission location and of the meteorological conditions during emission and subsequent transport pathways towards different chemical regimes: high photochemical O_3 production occurs for transport pathways towards lower latitudes and altitudes, whereas only moderate O_3 production is found for transport pathways towards high altitudes and latitudes.

In order to better understand how the prevailing meteorology during an emission event and the subsequent transport pathways influence the O_3 CCFs, we analyse in detail where and when the bulk O_3 increase occurred for trajectories started in different meteorological situations. In the following, this is referred to as the O_3 gain latitude, altitude, and time. We identify three regions, which are exemplarily studied for W1, W3, W4, and W5, having either a pronounced high-pressure ridge (W3 and W4) or a zonally oriented jet stream (W1, W4, and W5) in common. The regions discriminated in this analysis are

- in the high-pressure ridge,
- west of the high-pressure ridge, and
- at high O_3 CCF regions near the jet stream

(see Appendix A for their definition). Figure 10 (left) shows the probability density function of the O_3 gain latitude for W1, W3, W4 and W5 based on 300 and 450 trajectories for the high-pressure ridge and jet-stream-related situations, respectively (see Table A1 and black dots in Fig. 2 for the trajectory starting points). All three meteorological situations show a wide spread of the ozone gain latitude between 0 and $60^\circ N$. However, there is a clear difference in the probability density function (PDFs) of the main ozone gain latitude (Fig. 10, left) for the trajectories starting in the area of the high-pressure ridge with a major mode at $20^\circ N$ (red curve) compared to the trajectories starting west of the high-pressure ridge with a major mode at $40^\circ N$ (blue curve). Emissions released within the high-pressure ridge have a larger probability to be transported towards the tropics compared to trajectories starting at the same latitude but west of

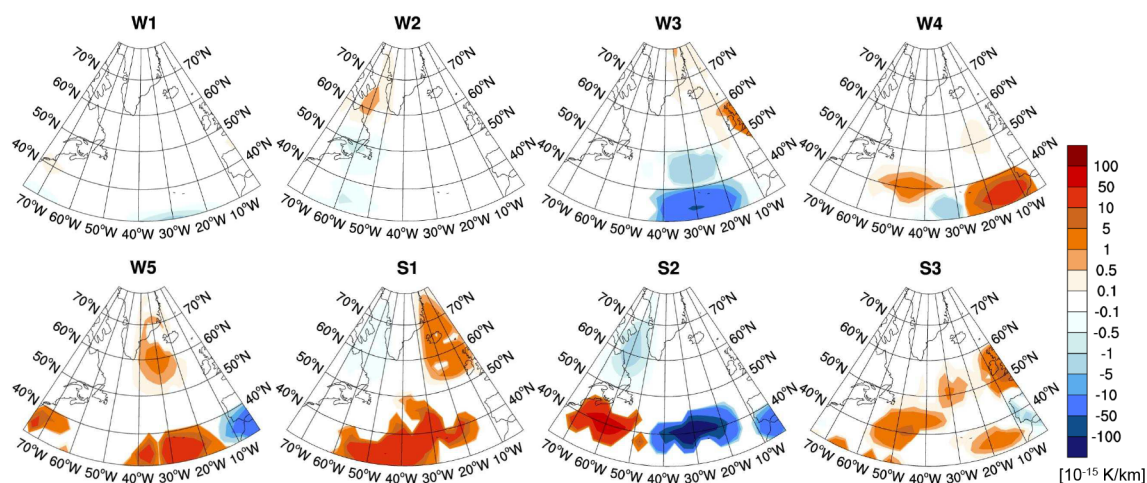


Figure 7. Climate change functions of contrail cirrus at 250 hPa in 10^{-15} K per kilometre flown for eight representative weather situations and an emission at 12:00 UTC. CCFs for other pressure levels and times investigated in this study are presented in the Supplement.

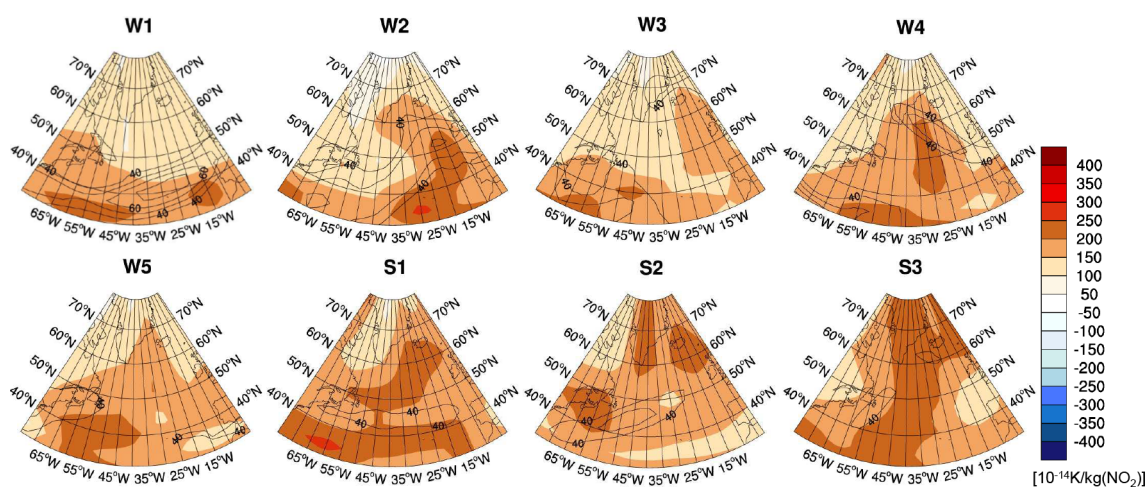


Figure 8. Climate change functions of aviation-induced O_3 at 250 hPa in 10^{-14} K per kilogram of NO_2 for eight representative weather situations and an emission at 12:00 UTC. The isolines show the wind speed in metres per second ($> 40 \text{ m s}^{-1}$) at 250 hPa. CCFs for other pressure levels and times investigated in this study are presented in the Supplement.

the ridge, which stay at higher latitudes or are transported even northwards. The ozone gain latitude of trajectories starting west of the high-pressure ridge is close to the latitude of the emission. The ozone gain altitude and time (Fig. 10, middle and right) show a main mode at 6 km and 10 d for trajectories starting in the high-pressure ridge (red curve) and 7.5 km and ~ 15 d for trajectories starting west of the ridge (blue curve), respectively. Note that the shape of the PDFs differs significantly. The air parcels starting in the high-pressure ridge experience the ozone gain earlier and at lower altitudes than the air parcels starting west of the ridge, which experience ozone gain for a much longer period and at higher altitudes. As known from general meteorology, the transport pathways are controlled by the location of air parcels relative to the Rossby waves, leading to transport into different

chemical regimes, such as the tropical mid-troposphere or the mid- to high-latitude lowermost stratosphere, which are characterized by a high or low chemical activity, respectively. In a companion paper (Rosanka et al., 2020), the interdependency of the time and magnitude of the O_3 maximum on the containment of air parcels within high-pressure systems during emission has been further analysed. They detected a high correlation of early O_3 maxima when air parcels were released within high-pressure systems and found that high O_3 changes were only possible for early O_3 maxima. The O_3 CCF values in the vicinity of the jet stream are of similar magnitude as the values in the area of the high-pressure ridges. The PDFs of the main ozone gain latitude, altitude, and time of the trajectories starting in the vicinity of the jet stream (Fig. 10, black line) look similar to the PDFs of the region west of the

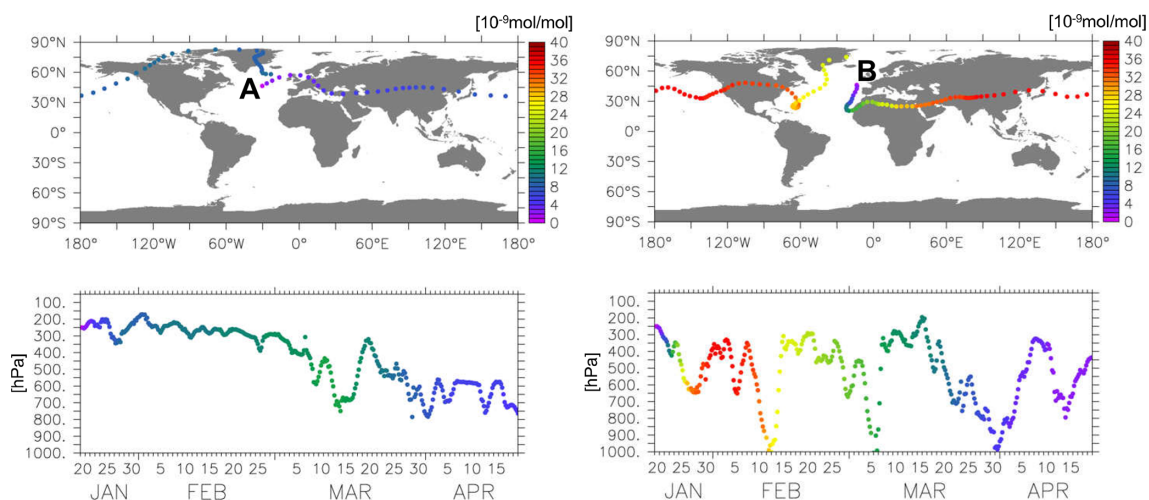


Figure 9. Evolution of the ozone mixing ratio along air parcel trajectories for two different emission locations in weather pattern W3: A (45° N and 30° W, left), which is west of the high-pressure ridge, and B (45° N and 15° W, right), which is in the high-pressure ridge. Top: geographical location of the air parcel in 6 h intervals; the colour indicates the ozone mixing ratio [10^{-9} mol mol $^{-1}$]. Bottom: temporal evolution of the altitude of the air parcels. For reasons of clarity, the top panels show a shorter period than the bottom panels (A: ~ 15 d, B: ~ 27 d, i.e. the time in which the air parcel surrounded the earth once).

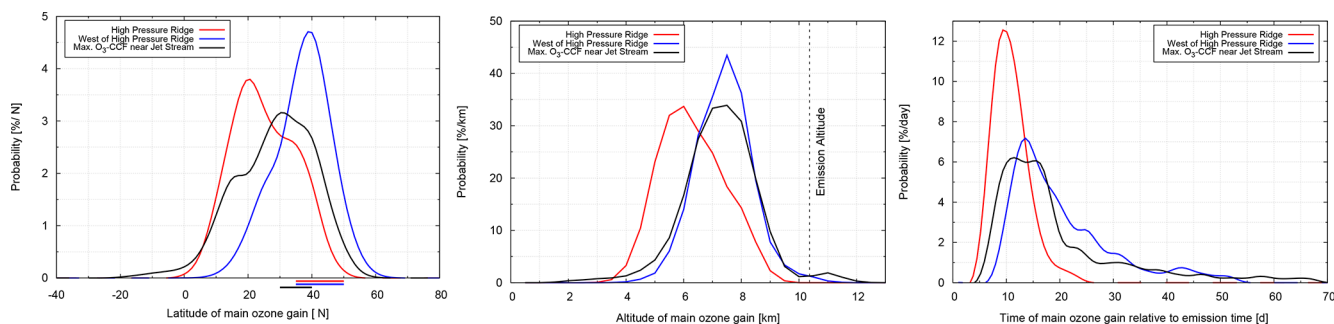


Figure 10. Weighted probability density function of the main ozone gain latitude (left), altitude (middle), and time (right) for three different regions: in the high-pressure ridge (red), west of the high-pressure ridge (blue), and in the area of large O_3 CCF values near the jet stream (black) (for information on regions and weighting, see Appendix A, Table A1, and black dots in Fig. 2). The location of emission release is indicated by bars.

high-pressure ridges but show a large variability among the three weather patterns W1, W4, and W5 (not shown). For example, in W4, the jet stream is split (Fig. 2), which leads to a bimodal distribution (15 and 35° N) of the main ozone gain latitude, whereas in W1, which is characterized by a strong zonal jet stream, the PDF is unimodal and very narrow, with a peak at 30° N. However, in both situations (W1 and W4), most air parcels released within the jet are transported to lower altitudes within the first 2 weeks after emission. This indicates that, similar to the findings for high-pressure systems, these air parcels are quickly transported into regions of high chemical efficiency, resulting in a high climate impact. This again emphasizes the importance of analysing location- and weather-dependent aviation effects and at the same time supports the potential of finding similarities between corresponding weather patterns.

Figure 11 shows the combined CCFs induced by nitrogen oxide (NO_x) emissions from aviation. Aviation emissions of NO_x cause an increase of O_3 , a decrease of CH_4 , and a methane-induced decrease of O_3 (PMO); in the following we denote these combined effects as total NO_x effect. The total NO_x effect is a combination of increased and reduced warming climate effects of similar magnitude. Depending on the size of the individual effects, the total NO_x CCF may be either positive or negative. Similarities between the pattern of NO_x CCF and the weather pattern (Fig. 2) are found, with high positive values in the area of the jet stream and in the area of high-pressure ridges and low or even negative CCFs at high latitudes and in the area of low-pressure troughs. The variability of the pattern is somewhat less pronounced than for O_3 . Total NO_x effects show a minimum at ~ 250 hPa, increasing towards higher and lower altitudes, with a higher

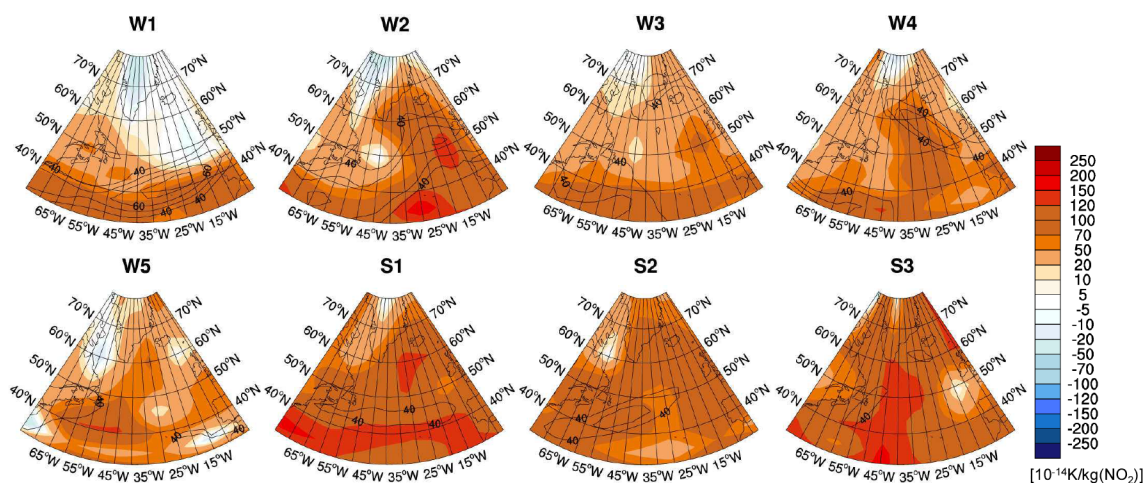


Figure 11. Climate change functions of aviation-induced total NO_x ($\text{O}_3 + \text{CH}_4 + \text{PMO}$) at 250 hPa in 10^{-14} K per kilogram of NO_2 for eight representative weather situations and an emission at 12:00 UTC. The isolines show the wind speed in metres per second ($> 40 \text{ m s}^{-1}$) at 250 hPa. CCFs for other pressure levels and times investigated in this study are presented in the Supplement.

(more warming) impact in summer than in winter (see Supplement). An emission release at different times of the day (06:00, 12:00, 18:00 UTC) was found to be negligible, and almost identical CCF results were obtained for O_3 and total NO_x .

4.3 Water vapour effects

Figure 12 shows the CCFs for H_2O in terms of ATR20 for all weather situations exemplarily at 250 hPa for an emission time of 12:00 UTC. For this emission altitude (250 hPa), the climate impact varies by approximately 1 order of magnitude. The variability shows a pattern which clearly reflects the weather situations shown in Fig. 2. Where the high-pressure ridges induce a higher tropopause altitude (in W2, W3, W4, S3), the emitted H_2O will rain out more quickly, thus having a shorter residence time, which leads to a lower climate impact of H_2O emissions compared to the regions east or west of the high-pressure ridge. Conversely, low-pressure troughs correspond to a lower tropopause; thus emissions are released closer to or even in the lowermost stratosphere, where they have a longer residence time and thus a higher climate impact. In summer (S1, S2, S3), the H_2O CCF is considerably smaller than in the winter weather patterns because of a higher tropopause height, stronger convective overturning, and thus shorter H_2O lifetimes. In general, the distance of the emission altitude to the actual tropopause largely controls the climate impact of H_2O emissions, as will be discussed in Sect. 5. Generally, H_2O CCFs increase with height and are higher in winter than in summer (see Supplement). The time of emission release (06:00, 12:00, 18:00 UTC) was found to be negligible, and almost identical CCF results were obtained for H_2O .

5 Discussion

In the previous sections, we have shown that large weather-related differences of non- CO_2 aviation climate effects exist. We could identify systematic weather-related similarities. Regarding contrail cirrus, we found enhanced potential coverage in areas where large-scale lifting of air masses occurs. Close to the jet stream, low potential coverage was observed. These general findings are supported by the study of Irvine et al. (2012), who analysed the distribution of ice-supersaturated regions (ISSRs) in similar weather situations within 20 years of ERA-Interim data (European Centre for Medium-Range Weather Forecasts Reanalysis Interim data; Dee et al., 2011). The exact manifestation of potential contrail coverage varies with the characteristic features of the weather situation. In general, our findings correspond well with the potential contrail cirrus coverage simulated by Burkhardt et al. (2008), given that their numbers (17%–21%) for 230–275 hPa comprise only 30–60° N. Regarding contrail lifetimes, our mean lifetimes of 3.5 ± 5.3 h agree well with the estimates of Gierens and Vazquez-Navarro (2018), who determined the complete lifetime of persistent contrails to be 3.7 ± 2.8 h by applying an automatic tracking algorithm in combination with statistical methods to 1 year of Meteosat SEVIRI data over Europe and the North Atlantic. In their example, 80% of contrails had a lifetime smaller than 5 h, and 5% lived longer than 10 h. Figure 13 compares the cumulative probability density function of lifetimes of both studies, illustrating that in the present study, a comparably larger fraction of contrails has lifetimes below 3 h. Only the initial and the final stage of contrail lifetimes could be estimated by Gierens and Vazquez-Navarro (2018), as these stages are difficult to observe by satellite platforms. Ice water contents and optical depths for contrails of the REACT4C study were

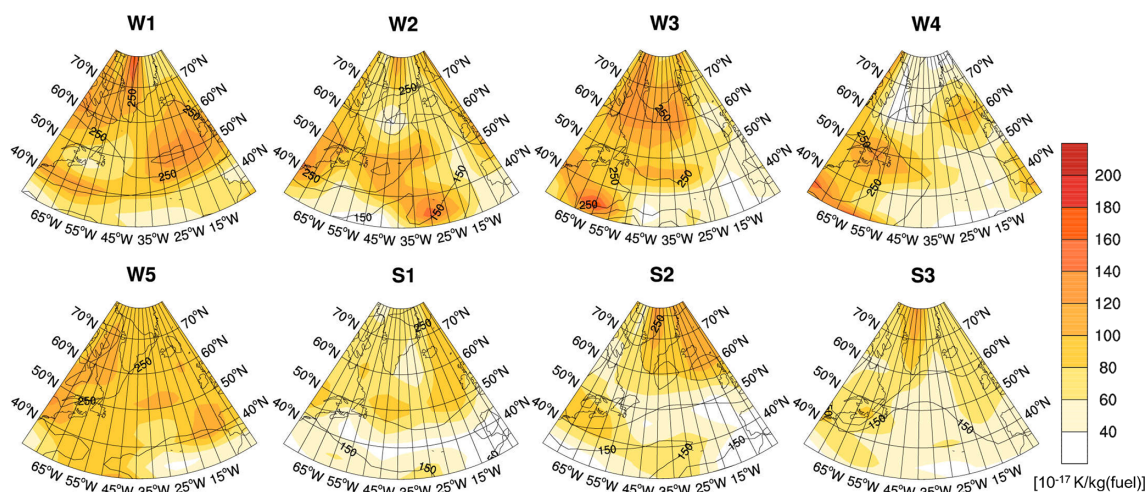


Figure 12. H₂O climate change functions for the eight individual weather situations and an emission at 12:00 UTC at 250 hPa. CCFs for other pressure levels and times investigated in this study are presented in the Supplement. The isolines show the height of the tropopause in hectopascals (hPa).

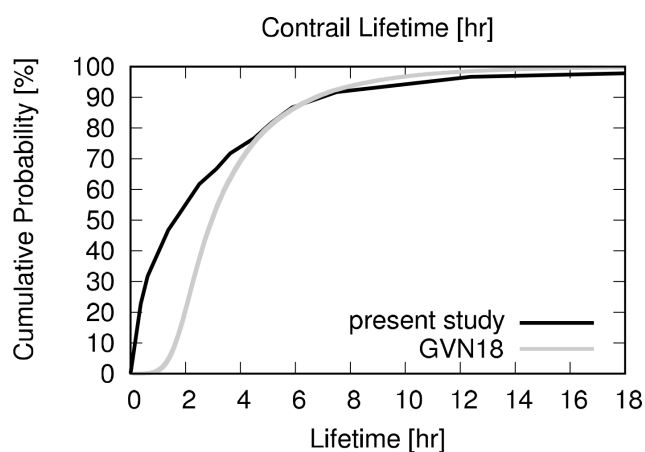


Figure 13. Cumulative probability of contrail lifetimes for all weather situations in comparison to Gierens and Vazquez-Navarro (2018) (i.e. GVN18).

already presented in Grewe et al. (2014b) and were found to compare well with other studies, e.g. Kärcher et al. (2009), Frömming et al. (2011), and Voigt et al. (2011).

Whether the climate impact of contrails and contrail cirrus is warming or cooling in the respective situation is complex and involves detailed knowledge about, for example, contrail optical properties, contrail lifetimes, solar zenith angle, ambient cloud coverage, and surface properties below the contrail (e.g. Schumann et al., 2012). In general, enhanced climate impact of contrail cirrus (irrespective of positive or negative) was detected south of the jet stream, in the vicinity of Greenland, and in areas with strong meridional transport, whereas comparably low contrail cirrus climate impact is found close to the jet stream. More detailed and smaller scale

structures of contrail formation areas cannot be resolved with the present model resolution. A higher spatial and temporal resolution of time regions and of the underlying atmospheric conditions would be favourable for future studies on contrail CCFs.

Regarding O₃ and total NO_x CCFs, we identified high positive values in the area of the jet stream and in the area of high-pressure ridges, whereas low or even negative CCFs were found at high latitudes and in the area of low-pressure systems. In general, the climate impact is higher in summer than in winter because of reduced photochemistry due to missing sunlight in winter. These findings are in qualitative agreement with earlier climatological studies showing higher responses for NO_x emissions at low latitudes and lower or even negative effects at high latitudes (e.g. Berntsen et al., 2005; Köhler et al., 2008, 2013; Grewe and Stenke, 2008) and comparable seasonal effects (e.g. Gauss et al., 2006). A newer study by Lund et al. (2017) also found largest effects of aviation NO_x for emissions in the tropics and subtropics and smaller effects for emissions at midlatitudes. They state that the sign and magnitude of total NO_x climate effects in such studies depend strongly on the chosen metric and time horizon. Furthermore, large inter-model differences exist in the change in methane lifetime per unit ozone change as discussed by, for example, Köhler et al. (2008) and Myhre et al. (2011). In comparison with studies regarding annual averages, the present study enables a representation of more detailed transport pathways, characteristic of synoptic weather patterns. The knowledge that can be gained from this study, focusing on synoptic weather patterns, is that not only the emission region is significant, but also, even more, the transport pathways from that emission region towards other chemical regimes. A correlation between the climatological response of O₃ and CH₄ and NO_x emissions has been shown

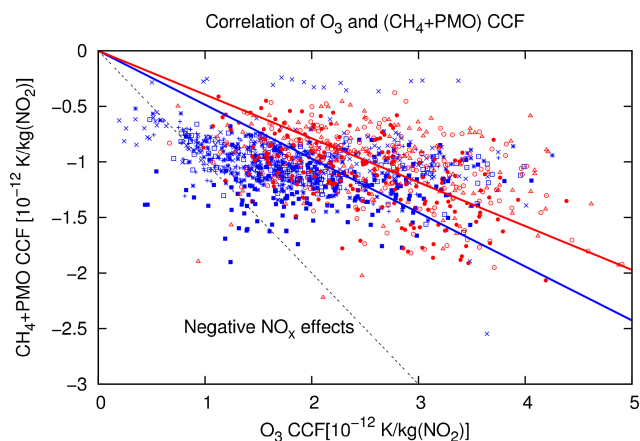


Figure 14. Correlation of O_3 CCFs and the CH_4 and PMO CCFs. The dashed line indicates the transition where the total NO_x effect becomes negative. The symbols indicate the different weather patterns (blue is winter; red is summer). The blue and red lines show a linear fit for winter and summer weather patterns, respectively.

in many studies (e.g. Lee et al., 2010; Holmes et al., 2013; Köhler et al., 2013). Our data demonstrate that this relation continues when regarding individual weather situations. Figure 14 shows the O_3 CCFs and the combined CH_4 –PMO CCFs for all weather situations. A clear correlation is found, indicating that actual weather influences both effects in a similar way, with large or small positive values of O_3 CCFs correlated with large or small negative CH_4 and PMO CCFs. However, the variability of the O_3 CCFs ($\pm 1.5 \times 10^{-12}$ K per kilogram of NO_2) is about a factor of 3 larger than the combined CH_4 –PMO variability ($\pm 0.5 \times 10^{-12}$ K per kilogram of NO_2).

The H_2O CCFs were also found to be closely related to the actual weather pattern. In regions with higher tropopause altitudes the emitted water vapour has a shorter atmospheric residence time and thus a lower climate impact, whereas in regions with lower tropopause height, the emitted water vapour has a longer residence time and a higher climate impact. In the summer situations, the H_2O CCFs are generally smaller than in winter because of enhanced convective activity (larger vertical mixing) and subsequent rainout of H_2O and a generally higher tropopause height. Figure 15 shows the correlation of H_2O CCFs to the emission altitude relative to the tropopause. The H_2O emission from 1 kg fuel occurring below the tropopause yields a warming of approximately 0.5×10^{-15} K, whereas the same emission above the tropopause leads to a warming of around 1 to 3×10^{-15} K. In general, the distance of the emission altitude to the actual tropopause largely controls the climate impact of H_2O emissions. The higher the water vapour emissions are released (relative to the tropopause), the longer it takes until this water vapour enters the troposphere and will eventually be rained out, i.e. the longer its residence time is. These findings are supported by earlier studies regarding the climate

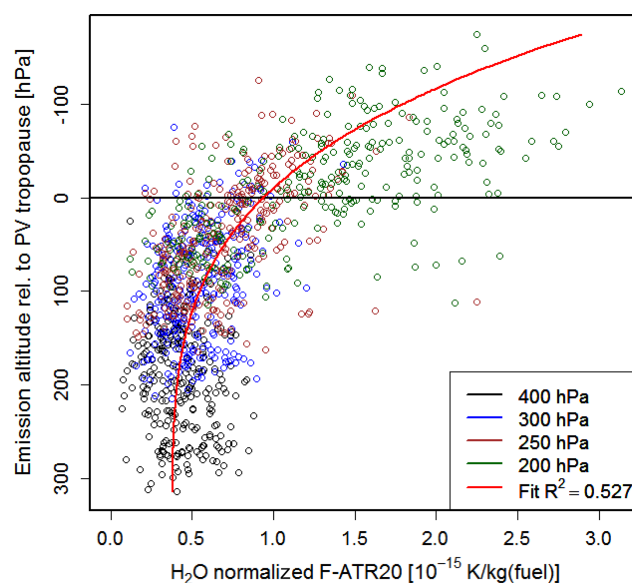


Figure 15. Correlation of water vapour climate change functions (kelvin (K) per kilogram of fuel) with emission altitude difference relative to the actual tropopause. Pressure levels of the various emission altitudes are distinguished by different colours. A fit function is indicated by the red line.

effect of water vapour emissions from aviation in a climatological sense (e.g. Grewe and Stenke, 2008; Fichter, 2009; Frömring et al., 2012; Wilcox et al., 2012).

Our findings are in agreement with earlier studies which investigated the altitude and latitude dependency of annual mean or seasonal non- CO_2 aviation effects (e.g. Gauss et al., 2006; Köhler et al., 2008, 2013; Grewe and Stenke, 2008; Fichter, 2009; Frömring et al., 2012). Furthermore, as far as comparable, our findings are also in qualitative agreement with studies which investigated the avoidance of contrails (e.g. Mannstein et al., 2005; Sridhar et al., 2011; Chen et al., 2012; Irvine et al., 2014; Zou et al., 2016; Hartjes et al., 2016; Yin et al., 2018a), although the present study does not optimize trajectories but is only setting the scene. These previous studies indicated a strong reduction potential but were only valid for the actual situation and could not be transferred to other situations.

The weather situations which were selected in our study occurred in the months December to February and June and July. Although our findings might be transferable to other seasons, future studies should look at special features which might occur in other months.

In the present study, we have explicitly excluded the direct and indirect climate impact of aviation aerosols. The status of knowledge on indirect aerosol effects is not considered to be mature enough to be included in such a study. This will be covered in future projects.

It is essential to note that uncertainties are associated with individual climate change functions presented in this study.

However, for the application of these data in terms of optimization of flight trajectories, not the exact value of climate impact is crucial but the relation of the individual components and their spatial and temporal variability. Grewe et al. (2014a) performed a detailed study on the sensitivity of routing changes with respect to uncertainties and potential errors in the climate change functions. Their sensitivity studies approximately cover the range of uncertainty of individual aviation climate effects as specified by Lee et al. (2010), and they investigated an increased variability of the individual atmospheric responses calculated. This had an effect on the weighting between the climate impact from NO_x and contrail cirrus. Grewe et al. (2014a) found differences in the reduction potentials but similar optimal routes. These sensitivity studies indicate a stable response in the shape of the cost-benefit analyses and the way air traffic is routed for climate impact.

The CCFs of the individual species show the sensitivity of the atmosphere to non- CO_2 aviation emissions. If flight trajectories were re-routed to reduce climate impact by avoiding the most sensitive regions, possible trade-offs between individual species need to be considered. With the present study, these trade-offs can be estimated in a consistent way as the effects of all species are represented by means of a consistent metric. For the first time, a comprehensive data set is available for various species, pressure levels, emission times, and a multitude of weather situations. During optimization, the characteristic effects of all species can be equally compared or individually be assigned with different weights. As a first step for a rough comparison, all CCFs are converted to kelvin (K) per kilogram of fuel. We multiply the contrail cirrus CCF by a typical specific range value for transatlantic flights of 0.16 km per kilogram of fuel (Graver and Rutherford, 2018, and Florian Linke, Deutsches Zentrum für Luft- und Raumfahrt, DLR, personal communication, 2020). Similarly, the total NO_x CCF is converted using a typical emissions index of NO_x of 13 g NO_2 per kilogram of fuel (Penner et al., 1999). Figure 16 shows the merged CCFs of contrail cirrus, total NO_x , and H_2O exemplarily for weather situation S2 at 250 hPa and 12:00 UTC. When evaluating the individual components of the merged CCFs, it is clearly revealed that contrail cirrus and O_3 CCFs are the dominating non- CO_2 effects. A hypothetical climate-optimized transatlantic flight (which will stay on this pressure level for simplification) would certainly try to avoid the area with high positive CCFs in the western Atlantic around 40°N , which is due to warming contrail cirrus and warming total NO_x effects. Further, this flight trajectory will probably find a compromise between avoiding long distances through enhanced climate warming areas and at the same time avoiding long detours as these would induce a penalty with respect to CO_2 CCF. However, situations are conceivable in which extensive areas with cooling contrails occur (similar to the negative CCF area in the central Atlantic), which flight trajectories might purposely seek during optimization to minimize their overall cli-

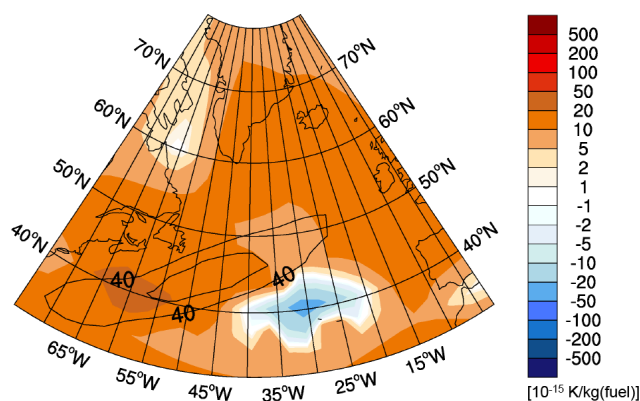


Figure 16. Merged climate change functions in 10^{-15} K per kilogram of fuel of aviation-induced total NO_x , contrail cirrus, and H_2O at 250 hPa exemplarily for weather situation S2 for an emission at 12:00 UTC.

mate impact. We emphasize that this is a very simplified example to illustrate the concept. The optimization of weather-dependent flight trajectories with respect to minimum climate impact is much more complex. However, such an optimization goes clearly beyond the scope of the present study. Nonetheless, the data from the present study are a comprehensive and valuable basis for weather-dependent flight trajectory optimization with minimum climate impact. Some of the studies, based on the present data, have already been published (e.g. Grewe et al., 2014a; Niklass et al., 2017; Yin et al., 2018b; Yamashita et al., 2020), others are in preparation.

Common features of the non- CO_2 CCFs facilitate the usage of our results for the development of more generalized algorithmic climate change functions (aCCFs). If CCFs were intended to be used for actual climate optimal flight planning, it would be necessary to predict the sign and magnitude of individual CCFs for the actual weather situation. Due to excessive use of computing time, it is not possible to calculate CCFs in detail for any actual situation. A procedure would be necessary to bypass detailed simulations. On the basis of specific CCFs from the present study, more generic climate change functions, so-called algorithmic climate change functions, were developed. These algorithms facilitate the prediction of CCFs by means of instantaneous meteorological data from weather forecasts without the necessity of computationally extensive recalculation of CCFs by means of chemistry–climate model simulations. This was the aim of the related studies by Van Manen and Grewe (2019) and Yin et al. (2021). A number of assumptions and simplifications were necessary for such an approach. Nevertheless, algorithms have been devised for the prediction of O_3 , CH_4 , H_2O , and contrail cirrus CCFs. These aCCFs would facilitate weather-related climate-optimized planning of flight trajectories for any weather situation. Such a modelling study has been performed by, for example, Yamashita et al. (2020),

who implemented the aCCFs in a flight planning tool, to optimize flight trajectories with regard to various objective functions.

6 Summary and conclusions

We investigated the influence of different weather situations on the climate impact of non-CO₂ aviation emissions. Our results are 4D climate change functions, which describe the climate impact of local emissions of NO_x and H₂O, affecting the formation of contrail cirrus and the mixing ratios of the greenhouse gases O₃, CH₄, and H₂O. We studied the impact of local emissions for eight different representative weather situations and for three points in time per day, resolving the temporal evolution of the weather system. The main objective was to derive systematic relationships between the emission location, the prevailing weather situation during emission, and the resulting aviation climate impact. The model configuration and methodology, which have been employed in this research paper, for generating spatially and temporally resolved information on the sensitivity of the atmosphere to local aviation emissions are, to the best of our knowledge, unique.

For all non-CO₂ species included in this study, we found distinct weather-related differences in their associated CCFs. We found an enhanced significance of the position of emission release in relation to high-pressure systems, to the jet stream, to the altitude of the tropopause, and to polar night. Regarding chemical effects of aviation NO_x emissions, we find that not only the emission region is relevant; in fact, the main driver for enhanced climate impact sensitivity is transport pathways of emissions within the first week(s) after emission. If emissions are released west of a high-pressure system, they stay or are transported to high latitudes, resulting in minor O₃ production. If emissions are released in a high-pressure system, they are transported towards lower altitudes and latitudes and experience strong photochemical O₃ production, causing enhanced climate impact. The transport pathways are adequately represented in the present study, and weather patterns compare very well with the classification using ERA-Interim data (Irvine et al., 2013). The climate impact of H₂O emissions is largely controlled by the distance to the tropopause, with emissions released close to the tropopause or even in the lowermost stratosphere, causing the strongest climate impact. Diurnal effects are negligible for aviation NO_x and H₂O emissions. Regarding contrail cirrus CCFs, the results are too diverse to be summarized easily. The main factor for contrail cirrus climate impact is ambient conditions during contrail formation and some hours after. The diurnal variation of insolation is crucial in combination with the lifetime of contrails as it has the potential to change the sign of contrail climate impact. Reproducing a higher degree of detail regarding the small-scale structure of contrails and contrail cirrus and their temporal variation could be im-

proved in future studies through enhanced spatial and temporal resolution. However, whether a smaller scale structure of contrail cirrus CCFs would have an impact on flight trajectory optimization has not yet been investigated.

The results of this study represent a comprehensive data set for studies aiming at weather-dependent flight trajectory optimization to reduce total climate impact. The dominating non-CO₂ effects were found to be contrail cirrus and impacts induced by NO_x emissions on average; however, this might deviate temporally and regionally. For an implementation of climate change functions in actual flight planning, it would be necessary to accurately predict the sign and magnitude of individual CCFs for the actual weather situation. This can possibly be pursued by means of more generic aCCFs, which facilitate the prediction of CCFs by means of instantaneous meteorological data (e.g. Matthes et al., 2017). These aCCFs have to be verified, and first verification results for the O₃ aCCFs are promising (Yin et al., 2018b). However, to improve the quality of these predictions, more knowledge has to be gained, particularly with respect to the transition of warming to cooling climate effects from contrail cirrus and total NO_x impacts. Further evaluation and quantitative estimates on uncertainties require additional comprehensive climate-chemistry simulations. Furthermore, better understanding of the trade-offs between different effects (e.g. transport versus chemistry) or different species is essential. It might also be useful to focus on evaluating what might be the most promising regions to bypass, in other words, where total climate impact is highest and easiest to avoid or at lowest additional cost. The CCFs presented in this study represent an indispensable data basis for climate-optimized flight planning. The potential implementation of such an approach faces several challenges; a roadmap of how to overcome these is elaborated in Grewe et al. (2017).

Appendix A: Calculation of the main ozone gain latitude, altitude, and time

The main ozone gain latitude (ϕ_j) of an emission location (identified with the index j) is defined as the mean latitude at which the air parcel trajectories experience most of the ozone increase. Accordingly, the main ozone altitude and time are defined as the mean altitude and time at which the air parcel trajectories experience most of the ozone increase, respectively. In the following, we exemplarily define how the ozone gain latitude is derived; the other quantities are obtained by replacing latitude by altitude and time, respectively. The air parcel trajectories (identified with the index i) will contribute different shares to the total ozone gain latitude. The ozone gain ($O_3^{\text{Gain}_i}(t)$) along an air parcel trajectory is defined as the increase in O_3 from the previous to the current time step t (for a decrease in O_3 , the ozone gain is set to 0). The contribution $A_{j,i}$ of a single trajectory i to the latitude of the main ozone gain (= ozone gain latitude) for the emission location j is given by

$$A_{j,i} = \int \frac{O_3^{\text{Gain}_i}(t) \cdot \phi_i(t)}{\sum_{i=1}^{50} \int O_3^{\text{Gain}_i}(t) dt} dt, \quad (\text{A1})$$

where $\phi_i(t)$ is the latitude of the trajectory i at time t . By taking the sum of the contributions $A_{j,i}$ of all trajectories i starting at emission location j , the latitude of the main ozone gain is

$$\phi_j = \sum_{i=1}^{50} A_{j,i}. \quad (\text{A2})$$

The weights ($w_{j,i}$) for each trajectory to the ozone gain latitude are calculated by combining Eqs. (A1) and (A2):

$$w_{j,i} = A_{j,i} / \phi_j. \quad (\text{A3})$$

A similar procedure is used to calculate the latitude of ozone gain for each single trajectory $\phi_{j,i}$:

$$\phi_{j,i} = \int \frac{O_3^{\text{Gain}_i}(t) \cdot \phi_i(t)}{\int O_3^{\text{Gain}_i}(t) dt} dt. \quad (\text{A4})$$

The main difference between ϕ_j and $\phi_{j,i}$ is the weighting of the latitude. For $\phi_{j,i}$ the ozone gain of a single trajectory is taken into account, whereas for ϕ_j the ozone gain of all trajectories starting at the emission region j is taken into account. Equations (A3) and (A4) define a data set containing the contribution and the latitudinal location of the main ozone gain for each trajectory. Based on these data, a weighted PDF is derived in Eq. (A5). For a bin size of $\Delta\phi$, a centre ϕ of this bin, and n air parcel trajectories ($i = 1, \dots, n$), which have their main ozone gain $\phi_{j,i}$ in this bin, the PDF is

$$\text{pdf}(\phi) = \frac{\sum_{j=1}^n w_{j,i}}{\sum w_{j,i} \cdot \Delta\phi}. \quad (\text{A5})$$

The sampling size of this PDF would be rather small if only a single emission location were taken into account (50 trajectories). In order to enhance the data basis, trajectories from various emission grid points are sampled for different meteorological features (high-pressure ridge, west of high-pressure ridge, and near jet stream). In case 1 (“high-pressure ridge”), the maximum of the O_3 CCFs is analysed for W3 and W4, which are both in the region of a high-pressure ridge. In case 2 (“west of high-pressure ridge”), the same weather situations (W3 and W4) are analysed, but the emission locations evaluated lie further west compared to the points of case 1. In this case, the O_3 CCFs are significantly lower. In both cases, the same emission latitudes are taken into account but different longitudes. The last case (“near jet stream”) considers the location of high O_3 CCFs in the vicinity of the jet stream. For this case, weather patterns W1, W4, and W5 are analysed. A summary of all emission locations taken into account is given in Table A1. Results are discussed in Sect. 4.2.

Table A1. Overview of all considered locations for the weighted probability density functions.

High-pressure ridge		West of high-pressure ridge		Max. O_3 CCF near jet stream		
W3	W4	W3	W4	W1	W4	W5
40° N, 15° W	35° N, 30° W	40° N, 30° W	35° N, 75° W	35° N, 60° W	30° N, 60° W	40° N, 75° W
45° N, 15° W	40° N, 30° W	45° N, 30° W	40° N, 60° W	35° N, 45° W	30° N, 45° W	40° N, 60° W
50° N, 15° W	45° N, 30° W	50° N, 30° W	45° N, 45° W	35° N, 15° W	30° N, 30° W	40° N, 45° W

Code and data availability. The Modular Earth Submodel System (MESSy) is continuously further developed and applied by a consortium of institutions. The usage of MESSy and access to the source code is licenced to all affiliates of institutions which are members of the MESSy consortium. Institutions can become a member of the MESSy consortium by signing the MESSy Memorandum of Understanding. More information can be found on the MESSy consortium website (<http://www.messy-interface.org>, last access: 11 June 2021). The results presented here have been obtained with a modified MESSy version 2.42; these modifications became part of the official release of MESSy version 2.50. The results presented in this work are archived at DKRZ and are available on request. A part of the data is available via the REACT4C project home page (<https://www.react4c.eu/>, Grewe et al., 2021).

Supplement. The supplement related to this article is available online at: <https://doi.org/10.5194/acp-21-9151-2021-supplement>.

Author contributions. CF, VG, and SM designed the study. CF and PJ developed the relevant EMAC submodels, with input from VG and SB. CF and SB performed the EMAC simulations. AH calculated the CCFs from the EMAC output, with contributions from CF and VG. CF analysed the data, with contributions from VG, SR, and JVM. CF prepared the manuscript, with contributions from all co-authors.

Competing interests. Author Patrick Jöckel is a member of the editorial board of the journal.

Acknowledgements. Computational resources were made available by the German Climate Computing Center (DKRZ) through support from the German Federal Ministry of Education and Research (BMBF) and by the Leibniz-Rechenzentrum (LRZ). We gratefully acknowledge helpful discussions with Emma A. Klingaman (formerly Irvine) (University of Reading), Ruben R. de Leon (Manchester Metropolitan University), Keith Shine (University of Reading), and Katrin Dahlmann (DLR). We thank Helmut Ziereis (DLR – internal review) for many helpful comments.

Financial support. This research has been supported by the FP7 project REACT4C (React for climate; <http://www.react4c.eu/>, last access: 11 June 2021) and the European Union 7th Framework Programme (grant no. ACP8-GA-2009-233772).

Review statement. This paper was edited by Jayanarayanan Kuttipurath and reviewed by two anonymous referees.

References

- Aamaas, B., Peters, G. P., and Fuglestedt, J. S.: Simple emission metrics for climate impacts, *Earth Syst. Dynam.*, 4, 145–170, <https://doi.org/10.5194/esd-4-145-2013>, 2013.
- ACARE: Advisory Council for Aviation Research and Innovation in Europe (ACARE), <https://www.acare4europe.org/> (last access: 20 May 2020), 2020.
- Berntsen, T., Fuglestedt, J., Joshi, M., Shine, K., Stuber, N., Ponater, M., Sausen, R., Hauglustaine, D., and Li, L.: Response of climate to regional emissions of ozone precursors: sensitivities and warming potentials, *Tellus B*, 57, 283–304, <https://doi.org/10.1111/j.1600-0889.2005.00152.x>, 2005.
- Brasseur, G. P.: ACCRI – A Report on the way forward based on the review of research gaps and priorities, ACCRI – Aviation Climate Change Research Initiative, <http://www.faa.gov> (last access: June 2021), 2008.
- Brasseur, G. P., Gupta, M., Anderson, B. E., Balasubramanian, S., Barrett, S., Duda, D., Fleming, G., Forster, P. M., Fuglestedt, J., Gettelman, A., Halthore, R. N., Jacob, S. D., Jacobson, M. Z., Khodayari, A., Liou, K.-N., Lund, M. T., Miake-Lye, R. C., Minnis, P., Olsen, S., Penner, J. E., Prinn, R., Schumann, U., Selkirk, H. B., Sokolov, A., Unger, N., Wolfe, P., Wong, H.-W., Wuebbles, D. W., Yi, B., Yang, P., and Zhou, C.: Impact of Aviation on Climate FAA’s Aviation Climate Change Research Initiative (ACCRI) Phase II, *B. Am. Meteorol. Soc.*, 97, 561–583, <https://doi.org/10.1175/BAMS-D-13-00089.1>, 2016.
- Brinkop, S. and Jöckel, P.: ATTLA 4.0: Lagrangian advective and convective transport of passive tracers within the ECHAM5/MESSy (2.53.0) chemistry–climate model, *Geosci. Model Dev.*, 12, 1991–2008, <https://doi.org/10.5194/gmd-12-1991-2019>, 2019.
- Burkhardt, U. and Kaercher, B.: Process-based simulation of contrail cirrus in a global climate model, *J. Geophys. Res.-Atmos.*, 114, D16201, <https://doi.org/10.1029/2008JD011491>, 2009.
- Burkhardt, U., Kärcher, B., Ponater, M., Gierens, K., and Gettelman, A.: Contrail cirrus supporting areas in model and observations, *Geophys. Res. Lett.*, 35, L16808, <https://doi.org/10.1029/2008GL034056>, 2008.
- Chen, N. Y., Sridhar, B., and Ng, H. K.: Tradeoff Between Contrail Reduction and Emissions in United States National Airspace, AIAA Guidance, Navigation and Control Conference, Toronto, Canada, 2–6 August 2010, *J. Aircraft*, 49, 1367–1375, <https://doi.org/10.2514/1.C031680>, 2012.
- Dahlmann, K.: A method for efficient evaluation of measures for climate optimization of air traffic (published in German), PhD thesis, DLR-Forschungsbericht 2012-05, Cologne, Germany, (ISSN 1434-8454), 2012.
- Deckert, R., Jöckel, P., Grewe, V., Gottschaldt, K.-D., and Hoor, P.: A quasi chemistry-transport model mode for EMAC, *Geosci. Model Dev.*, 4, 195–206, <https://doi.org/10.5194/gmd-4-195-2011>, 2011.
- Dee, D. P., Uppala, S. M., Simmons, A. J., Berrisford, P., Poli, P., Kobayashi, S., Andrae, U., Balmaseda, M. A., Balsamo, G., Bauer, P., Bechtold, P., Beljaars, A. C. M., van de Berg, L., Bidlot, J., Bormann, N., Delsol, C., Dragani, R., Fuentes, M., Geer, A. J., Haimberger, L., Healy, S. B., Hersbach, H., Holm, E. V., Isaksen, L., Kallberg, P., Köhler, M., Matricardi, M., McNally, A. P., Monge-Sanz, B. M., Morcrette, J. J., Park, B. K., Peubey, C., de Rosnay, P., Tavolato, C., Thepaut, J. N., and Vitart, F.: The

- ERA-Interim reanalysis: configuration and performance of the data assimilation system, *Q. J. Roy. Meteor. Soc.*, 137, 553–597, <https://doi.org/10.1002/qj.828>, 2011.
- Dietmüller, S., Jöckel, P., Tost, H., Kunze, M., Gellhorn, C., Brinkop, S., Frömming, C., Ponater, M., Steil, B., Lauer, A., and Hendricks, J.: A new radiation infrastructure for the Modular Earth Submodel System (MESSy, based on version 2.51), *Geosci. Model Dev.*, 9, 2209–2222, <https://doi.org/10.5194/gmd-9-2209-2016>, 2016.
- European Commission: EU Emissions Trading System (EU ETS), https://ec.europa.eu/clima/policies/ets_en (last access: 20 May 2020), 2015.
- Fichter, C.: Climate impact of air traffic emissions in dependency of the emission location and altitude, PhD thesis, DLR-Forschungsbericht 2009-22, Cologne, Germany, ISSN 1434-8454, 2009.
- Fichter, C., Marquart, S., Sausen, R., and Lee, D.: The impact of cruise altitude on contrails and related radiative forcing, European Conference on Aviation, Atmosphere and Climate, Friedrichshafen, Germany, 30 June–3 July, 2003, *Meteorol. Z.*, 14, 563–572, <https://doi.org/10.1127/0941-2948/2005/0048>, 2005.
- Forster, P., Ramaswamy, V., Artaxo, P., Bernsten, T., Betts, R., Fahey, D. W., Haywood, J., Lean, J., Lowe, D. C., Myhre, G., Nganga, J., Prinn, R., Raga, G., Schulz, M., and Van Dorland, R.: Changes in atmospheric constituents and in radiative forcing, in: *Climate Change 2007: the Physical Science Basis. Contribution of Working Group I to the Fourth Assessment Report of the Intergovernmental Panel on Climate Change*, edited by: Solomon, S., Qin, D., Manning, M., Marquis, M., Averyt, K., Tignor, M. M. B., LeRoy Miller Jr., H., and Chen, Z., Cambridge University Press, Cambridge, 2007.
- Friedlingstein, P., O’Sullivan, M., Jones, M. W., Andrew, R. M., Hauck, J., Olsen, A., Peters, G. P., Peters, W., Pongratz, J., Sitch, S., Le Quééré, C., Canadell, J. G., Ciais, P., Jackson, R. B., Alin, S., Aragão, L. E. O. C., Armeth, A., Arora, V., Bates, N. R., Becker, M., Benoit-Cattin, A., Bittig, H. C., Bopp, L., Bultan, S., Chandra, N., Chevallier, F., Chini, L. P., Evans, W., Florentie, L., Forster, P. M., Gasser, T., Gehlen, M., Gilfillan, D., Gkritzalis, T., Gregor, L., Gruber, N., Harris, I., Hartung, K., Haverd, V., Houghton, R. A., Ilyina, T., Jain, A. K., Joetzer, E., Kadono, K., Kato, E., Kitidis, V., Korsbakken, J. I., Landschützer, P., Lefèvre, N., Lenton, A., Lienert, S., Liu, Z., Lombardozzi, D., Marland, G., Metzl, N., Munro, D. R., Nabel, J. E. M. S., Nakaoka, S.-I., Niwa, Y., O’Brien, K., Ono, T., Palmer, P. I., Pierrot, D., Poulter, B., Resplandy, L., Robertson, E., Rödenbeck, C., Schwinger, J., Séférian, R., Skjelvan, I., Smith, A. J. P., Sutton, A. J., Tanhua, T., Tans, P. P., Tian, H., Tilbrook, B., van der Werf, G., Vuichard, N., Walker, A. P., Wanninkhof, R., Watson, A. J., Willis, D., Wiltshire, A. J., Yuan, W., Yue, X., and Zaehle, S.: *Global Carbon Budget 2020*, *Earth Syst. Sci. Data*, 12, 3269–3340, <https://doi.org/10.5194/essd-12-3269-2020>, 2020.
- Frömming, C., Ponater, M., Burkhardt, U., Stenke, A., Pechtl, S., and Sausen, R.: Sensitivity of contrail coverage and contrail radiative forcing to selected key parameters, *Atmos. Environ.*, 45, 1483–1490, <https://doi.org/10.1016/j.atmosenv.2010.11.033>, 2011.
- Frömming, C., Ponater, M., Dahlmann, K., Grewe, V., Lee, D. S., and Sausen, R.: Aviation-induced radiative forcing and surface temperature change in dependency of the emission altitude, *J. Geophys. Res.*, 117, D19104, <https://doi.org/10.1029/2012JD018204>, 2012.
- Fuglestedt, J. S., Shine, K. P., Berntsen, T., Cook, J., Lee, D. S., Stenke, A., Skeie, R. B., Velders, G. J. M., and Waitz, I. A.: Transport impacts on atmosphere and climate: Metrics, *Atmos. Environ.*, 44, 4648–4677, <https://doi.org/10.1016/j.atmosenv.2009.04.044>, 2010.
- Gauss, M., Isaksen, I. S. A., Lee, D. S., and Søvde, O. A.: Impact of aircraft NO_x emissions on the atmosphere – trade-offs to reduce the impact, *Atmos. Chem. Phys.*, 6, 1529–1548, <https://doi.org/10.5194/acp-6-1529-2006>, 2006.
- Gierens, K. and Vazquez-Navarro, M.: Statistical analysis of contrail lifetimes from a satellite perspective, *Meteorol. Z.*, 27, 183–193, <https://doi.org/10.1127/metz/2018/0888>, 2018.
- Graver, B. and Rutherford, D.: White Paper on Transatlantic Airline Fuel Efficiency Ranking 2017, iCCT – The International Council on Clean Transportation, available at: <https://www.theicct.org> (last access: June 2021), 2018.
- Grewe, V.: A generalized tagging method, *Geosci. Model Dev.*, 6, 247–253, <https://doi.org/10.5194/gmd-6-247-2013>, 2013.
- Grewe, V. and Dahlmann, K.: How ambiguous are climate metrics? And are we prepared to assess and compare the climate impact of new air traffic technologies?, *Atmos. Environ.*, 106, 373–374, <https://doi.org/10.1016/j.atmosenv.2015.02.039>, 2015.
- Grewe, V. and Stenke, A.: AirClim: an efficient tool for climate evaluation of aircraft technology, *Atmos. Chem. Phys.*, 8, 4621–4639, <https://doi.org/10.5194/acp-8-4621-2008>, 2008.
- Grewe, V., Tsati, E., and Hoor, P.: On the attribution of contributions of atmospheric trace gases to emissions in atmospheric model applications, *Geosci. Model Dev.*, 3, 487–499, <https://doi.org/10.5194/gmd-3-487-2010>, 2010.
- Grewe, V., Champougny, T., Matthes, S., Frömming, C., Brinkop, S., Søvde, O. A., Irvine, E. A., and Halscheidt, L.: Reduction of the air traffic’s contribution to climate change: A REACT4C case study, *Atmos. Environ.*, 94, 616–625, <https://doi.org/10.1016/j.atmosenv.2014.05.059>, 2014a.
- Grewe, V., Frömming, C., Matthes, S., Brinkop, S., Ponater, M., Dietmüller, S., Jöckel, P., Garny, H., Tsati, E., Dahlmann, K., Søvde, O. A., Fuglestedt, J., Berntsen, T. K., Shine, K. P., Irvine, E. A., Champougny, T., and Hullah, P.: Aircraft routing with minimal climate impact: the REACT4C climate cost function modelling approach (V1.0), *Geosci. Model Dev.*, 7, 175–201, <https://doi.org/10.5194/gmd-7-175-2014>, 2014b.
- Grewe, V., Tsati, E., Mertens, M., Frömming, C., and Jöckel, P.: Contribution of emissions to concentrations: the TAGGING 1.0 submodel based on the Modular Earth Submodel System (MESSy 2.52), *Geosci. Model Dev.*, 10, 2615–2633, <https://doi.org/10.5194/gmd-10-2615-2017>, 2017.
- Grewe, V., Matthes, S., Søvde, A., and Shine, K.: REACT4C climate cost functions, available at: <https://www.react4c.eu/>, last access: 11 June 2021.
- Hartjes, S., Hendriks, T., and Visser, H.: Contrail Mitigation through 3D Aircraft Trajectory Optimization, in: 16th Aviation Technology, Integration, and Operations Conference, Washington, D. C., 13–17 June 2016, AIAA 2016-3908, <https://doi.org/10.2514/6.2016-3908>, 2016.
- Heymsfield, A. and Donner, L.: A Scheme for Parameterizing Ice-Cloud Water-Content in General-Circulation Models,

- J. Atmos. Sci., 47, 1865–1877, [https://doi.org/10.1175/1520-0469\(1990\)047<1865:ASFPIC>2.0.CO;2](https://doi.org/10.1175/1520-0469(1990)047<1865:ASFPIC>2.0.CO;2), 1990.
- Holmes, C. D., Prather, M. J., Søvde, O. A., and Myhre, G.: Future methane, hydroxyl, and their uncertainties: key climate and emission parameters for future predictions, *Atmos. Chem. Phys.*, 13, 285–302, <https://doi.org/10.5194/acp-13-285-2013>, 2013.
- Hoor, P., Borken-Kleefeld, J., Caro, D., Dessens, O., Endresen, O., Gauss, M., Grewe, V., Hauglustaine, D., Isaksen, I. S. A., Jöckel, P., Lelieveld, J., Myhre, G., Meijer, E., Olivie, D., Prather, M., Schnadt Poberaj, C., Shine, K. P., Staehelin, J., Tang, Q., van Aardenne, J., van Velthoven, P., and Sausen, R.: The impact of traffic emissions on atmospheric ozone and OH: results from QUANTIFY, *Atmos. Chem. Phys.*, 9, 3113–3136, <https://doi.org/10.5194/acp-9-3113-2009>, 2009.
- Houweling, S., Dentener, F., and Lelieveld, J.: The impact of nonmethane hydrocarbon compounds on tropospheric photochemistry, *J. Geophys. Res.-Atmos.*, 103, 10673–10696, <https://doi.org/10.1029/97JD03582>, 1998.
- ICAO: Carbon Offsetting and Reduction Scheme for International Aviation (CORSA), <https://www.icao.int/corsia> (last access: 20 May 2020), 2020.
- Irvine, E. A., Hoskins, B. J., and Shine, K. P.: The dependence of contrail formation on the weather pattern and altitude in the North Atlantic, *Geophys. Res. Lett.*, 39, L12802, <https://doi.org/10.1029/2012GL051909>, 2012.
- Irvine, E. A., Hoskins, B. J., Shine, K. P., Lunnon, R. W., and Froemming, C.: Characterizing North Atlantic weather patterns for climate-optimal aircraft routing, *Meteorol. Appl.*, 20, 80–93, <https://doi.org/10.1002/met.1291>, 2013.
- Irvine, E. A., Hoskins, B. J., and Shine, K. P.: A simple framework for assessing the trade-off between the climate impact of aviation carbon dioxide emissions and contrails for a single flight, *Environ. Res. Lett.*, 9, 064021, <https://doi.org/10.1088/1748-9326/9/6/064021>, 2014.
- Jöckel, P., Kerkweg, A., Pozzer, A., Sander, R., Tost, H., Riede, H., Baumgaertner, A., Gromov, S., and Kern, B.: Development cycle 2 of the Modular Earth Submodel System (MESSy2), *Geosci. Model Dev.*, 3, 717–752, <https://doi.org/10.5194/gmd-3-717-2010>, 2010.
- Jöckel, P., Tost, H., Pozzer, A., Kunze, M., Kirner, O., Brenninkmeijer, C. A. M., Brinkop, S., Cai, D. S., Dyroff, C., Eckstein, J., Frank, F., Garny, H., Gottschaldt, K.-D., Graf, P., Grewe, V., Kerkweg, A., Kern, B., Matthes, S., Mertens, M., Meul, S., Neumaier, M., Nützel, M., Oberländer-Hayn, S., Ruhnke, R., Runde, T., Sander, R., Scharffe, D., and Zahn, A.: Earth System Chemistry integrated Modelling (ESCI-Mo) with the Modular Earth Submodel System (MESSy) version 2.51, *Geosci. Model Dev.*, 9, 1153–1200, <https://doi.org/10.5194/gmd-9-1153-2016>, 2016.
- Kärcher, B., Burkhardt, U., Unterstrasser, S., and Minnis, P.: Factors controlling contrail cirrus optical depth, *Atmos. Chem. Phys.*, 9, 6229–6254, <https://doi.org/10.5194/acp-9-6229-2009>, 2009.
- Köhler, M., Radel, G., Dessens, O., Shine, K., Rogers, H., Wild, O., and Pyle, J.: Impact of perturbations to nitrogen oxide emissions from global aviation, *J. Geophys. Res.-Atmos.*, 113, D11305, <https://doi.org/10.1029/2007JD009140>, 2008.
- Köhler, M. O., Radel, G., Shine, K. P., Rogers, H. L., and Pyle, J. A.: Latitudinal variation of the effect of aviation NO_x emissions on atmospheric ozone and methane and related climate metrics, *Atmos. Environ.*, 64, 1–9, <https://doi.org/10.1016/j.atmosenv.2012.09.013>, 2013.
- Le Quere, C., Jackson, R. B., Jones, M. W., Smith, A. J. P., Abernethy, S., Andrew, R. M., De-Gol, A. J., Willis, D. R., Shan, Y., Canadell, J. G., Friedlingstein, P., Creutzig, F., and Peters, G. P.: Temporary reduction in daily global CO_2 emissions during the COVID-19 forced confinement, *Nat. Clim. Change*, 10, 647–653, <https://doi.org/10.1038/s41558-020-0797-x>, 2020.
- Lee, D. S., Pitari, G., Grewe, V., Gierens, K., Penner, J. E., Petzold, A., Prather, M. J., Schumann, U., Bais, A., Berntsen, T., Iachetti, D., Lim, L. L., and Sausen, R.: Transport impacts on atmosphere and climate: Aviation, *Atmos. Environ.*, 44, 4678–4734, <https://doi.org/10.1016/j.atmosenv.2009.06.005>, 2010.
- Lee, D., Fahey, D., Skowron, A., Allen, M., Burkhardt, U., Chen, Q., Doherty, S., Freeman, S., Forster, P., Fuglestedt, J., Gettelman, A., De Leon, R., Lim, L., Lund, M., Millar, R., Owen, B., Penner, J., Pitari, G., Prather, M., Sausen, R., and Wilcox, L. J.: The contribution of global aviation to anthropogenic climate forcing for 2000 to 2018, *Atmos. Environ.*, 244, 117834, <https://doi.org/10.1016/j.atmosenv.2020.117834>, 2021.
- Lund, M. T., Aamaas, B., Berntsen, T., Bock, L., Burkhardt, U., Fuglestedt, J. S., and Shine, K. P.: Emission metrics for quantifying regional climate impacts of aviation, *Earth Syst. Dynam.*, 8, 547–563, <https://doi.org/10.5194/esd-8-547-2017>, 2017.
- Lührs, B., Linke, F., Matthes, S., Grewe, V., and Yin, F.: Climate Impact Mitigation Potential of European Air Traffic in a Weather Situation with Strong Contrail Formation, *Aerospace*, 50, 1–15, <https://doi.org/10.3390/aerospace8020050>, 2021.
- Mannstein, H., Spichtinger, P., and Gierens, K.: A note on how to avoid contrail cirrus, *Transport Res. D-Tr. E.*, 10, 421–426, <https://doi.org/10.1016/j.trd.2005.04.012>, 2005.
- Marquart, S., Ponater, M., Mager, F., and Sausen, R.: Future Development of Contrail Cover, Optical Depth and Radiative Forcing: Impacts of Increasing Air Traffic and Climate Change, *J. Climate*, 16, 2890–2904, 2003.
- Matthes, S., Schumann, U., Grewe, V., Frömming, C., Dahlmann, K., Koch, A., and Mannstein, H.: Climate optimized air transport, in: *Atmospheric Physics: Background – Methods – Trends*, edited by: Schumann, 877, Springer, Berlin/Heidelberg, Germany, https://doi.org/10.1007/978-3-642-30183-4_44, 2012.
- Matthes, S., Grewe, V., Dahlmann, K., Frömming, C., Irvine, E., Lim, L., Linke, F., Lührs, B., Owen, B., Shine, K., Stromatas, S., Yamashita, H., and Yin, F.: A Concept for Multi-Criteria Environmental Assessment of Aircraft Trajectories, *Aerospace*, 4, 2890–2904, <https://doi.org/10.3390/aerospace4030042>, 2017.
- Matthes, S., Lührs, B., Dahlmann, K., Grewe, V., Linke, F., Yin, F., Klingaman, E., and Shine, K. P.: Climate-Optimized Trajectories and Robust Mitigation Potential: Flying ATM4E, *Aerospace*, 156, 1–15, <https://doi.org/10.3390/aerospace7110156>, 2020.
- Matthes, S., Lim, L., Burkhardt, U., Dahlmann, K., Dietmüller, S., Grewe, V., Haslerud, A., Hendricks, J., Owen, B., Pitari, G., Righi, M., and Skowron, A.: Mitigation of Non- CO_2 Aviation's Climate Impact by Changing Cruise Altitudes, *Aerospace*, 36, 1–20, <https://doi.org/10.3390/aerospace8020036>, 2021.
- Meerkötter, R., Schumann, U., Doelling, D., Minnis, P., Nakajima, T., and Tsushima, Y.: Radiative forcing by contrails, *Ann. Geophys.*, 17, 1080–1094, 1999.
- Myhre, G., Shine, K. P., Radel, G., Gauss, M., Isaksen, I. A., Tang, Q., Prather, M. J., Williams, J. E., van Velthoven,

- P., Dessens, O., Koffi, B., Szopa, S., Hoor, P., Grewe, V., Borken-Kleefeld, J., Bernsten, T. K., and Fuglestvedt, J. S.: Radiative forcing due to changes in ozone and methane caused by the transport sector, *Atmos. Environ.*, 45, 387–394, <https://doi.org/10.1016/j.atmosenv.2010.10.001>, 2011.
- Niklass, M., Gollnick, V., Lürs, B., Dahlmann, K., Frömming, C., Grewe, V., and Van Manen, J.: Cost-Benefit Assessment of Climate-Restricted Airspaces as an Interim Climate Mitigation Option, *Journal of Air Transportation*, 25, 27–38, <https://doi.org/10.2514/1.D0045>, 2017.
- Penner, J., Lister, D., Griggs, D., Dokken, D., and McFarland, M. E.: IPCC: Aviation and the global Atmosphere, Cambridge University Press, UK, 1999.
- Ponater, M., Marquart, S., and Sausen, R.: Contrails in a comprehensive global climate model: Parameterization and radiative forcing results, *J. Geophys. Res.-Atmos.*, 107, <https://doi.org/10.1029/2001JD000429>, 2002.
- Rädel, G. and Shine, K. P.: Radiative forcing by persistent contrails and its dependence on cruise altitudes, *J. Geophys. Res.-Atmos.*, 113, D07105, <https://doi.org/10.1029/2007JD009117>, 2008.
- Reithmeier, C. and Sausen, R.: ATTILA: atmospheric tracer transport in a Lagrangian model, *Tellus B*, 54, 278–299, 2002.
- Roeckner, E., Brokopf, R., Esch, M., Giorgetta, M., Hagemann, S., Kornblüeh, L., Manzini, E., Schlese, U., and Schulzweida, U.: Sensitivity of simulated climate to horizontal and vertical resolution in the ECHAM5 atmosphere model, *J. Climate*, 19, 3771–3791, <https://doi.org/10.1175/JCLI3824.1>, 2006.
- Rosanka, S., Frömming, C., and Grewe, V.: The impact of weather patterns and related transport processes on aviation's contribution to ozone and methane concentrations from NO_x emissions, *Atmos. Chem. Phys.*, 20, 12347–12361, <https://doi.org/10.5194/acp-20-12347-2020>, 2020.
- Sander, R., Baumgaertner, A., Gromov, S., Harder, H., Jöckel, P., Kerkweg, A., Kubistin, D., Regelin, E., Riede, H., Sandu, A., Taraborrelli, D., Tost, H., and Xie, Z.-Q.: The atmospheric chemistry box model CAABA/MECCA-3.0, *Geosci. Model Dev.*, 4, 373–380, <https://doi.org/10.5194/gmd-4-373-2011>, 2011.
- Sausen, R., Gierens, K., Ponater, M., and Schumann, U.: A diagnostic study of the global distribution of contrails part I: Present day climate, *Theor. Appl. Climatol.*, 61, 127–141, <https://doi.org/10.1007/s007040050058>, 1998.
- Schumann, U.: On conditions for contrail formation from aircraft exhausts, *Meteorol. Z.*, 5, 4–23, <https://doi.org/10.1127/metz/5/1996/4>, 1996.
- Schumann, U., Mayer, B., Graf, K., and Mannstein, H.: A Parametric Radiative Forcing Model for Contrail Cirrus, *J. Appl. Meteorol. Clim.*, 51, 1391–1406, <https://doi.org/10.1175/JAMC-D-11-0242.1>, 2012.
- Schwartz Dallara, E., Kroo, I. M., and Waitz, I. A.: Metric for Comparing Lifetime Average Climate Impact of Aircraft, *AIAA J.*, 49, 1600–1613, <https://doi.org/10.2514/1.J050763>, 2011.
- Shine, K., Derwent, R., Wuebbles, D., and Morcrette, J.-J.: Radiative forcing of climate, in: *Climate Change: The IPCC Scientific Assessment (1990)*, Report prepared for the Intergovernmental Panel on Climate Change by Working Group I, edited by: Houghton, J., Jenkins, G., and Ephraums, J., 410, Cambridge University Press, Cambridge, Great Britain, New York, USA and Melbourne, Australia, 1990.
- Sridhar, B., Ng, H. K., and Chen, N. Y.: Aircraft Trajectory Optimization and Contrails Avoidance in the Presence of Winds, 10th AIAA Aviation Technology, Integration, and Operations (ATIO) Conference, Ft Worth, TX, 13–15 September 2010, *J. Guid. Control Dynam.*, 34, 1577–1583, <https://doi.org/10.2514/1.53378>, 2011.
- Van Manen, J. and Grewe, V.: Algorithmic climate change functions for the use in eco-efficient flight planning, *Transport Res. D-Tr. E.*, 67, 388–405, <https://doi.org/10.1016/j.trd.2018.12.016>, 2019.
- Voigt, C., Schumann, U., Jessberger, P., Jurkat, T., Petzold, A., Gayet, J. F., Kraemer, M., Thornberry, T., and Fahey, D. W.: Extinction and optical depth of contrails, *Geophys. Res. Lett.*, 38, L11806, <https://doi.org/10.1029/2011GL047189>, 2011.
- Wilcox, L. J., Shine, K. P., and Hoskins, B. J.: Radiative forcing due to aviation water vapour emissions, *Atmos. Environ.*, 63, 1–13, <https://doi.org/10.1016/j.atmosenv.2012.08.072>, 2012.
- Yamashita, H., Yin, F., Grewe, V., Jöckel, P., Matthes, S., Kern, B., Dahlmann, K., and Frömming, C.: Newly developed aircraft routing options for air traffic simulation in the chemistry–climate model EMAC 2.53: AirTraf 2.0, *Geosci. Model Dev.*, 13, 4869–4890, <https://doi.org/10.5194/gmd-13-4869-2020>, 2020.
- Yin, F., Grewe, V., Frömming, C., and Yamashita, H.: Impact on flight trajectory characteristics when avoiding the formation of persistent contrails for transatlantic flights, *Transport Res. D-Tr. E.*, 65, 466–484, <https://doi.org/10.1016/j.trd.2018.09.017>, 2018a.
- Yin, F., Grewe, V., van Manen, J., Yamashita, H., Linke, F., and Lührs, B.: Verification of the ozone algorithmic climate change functions for predicting the short-term NO_x effects from aviation en-route, conference paper: ICRAT 2018, 2018b.
- Yin, F., Grewe, V., van Manen, J., Irvine, E., Shine, K., Lührs, B., Linke, F., Lim, L., Matthes, S., and Stromatas, S.: Predicting the climate impact of aviation en-route: The algorithmic climate change function sub model ACCF V1.0 of EMAC 2.53, in preparation, 2021.
- Zou, B., Buxi, G. S., and Hansen, M.: Optimal 4-D Aircraft Trajectories in a Contrail-sensitive Environment, *Netw. Spat. Econ.*, 16, 415–446, <https://doi.org/10.1007/s11067-013-9210-x>, 2016.